SLAC–PUB–5160 Rev.
March 1990
(T/E)

HADRON PRODUCTION IN e^+e^- ANNIHILATION FROM $\sqrt{s}$ = 5.0 TO 7.4 GeV

C. Edwards,(") R. Partridge,(*) C. Peck, and F. C. Porter
Physics Department, California Institute of Technology, Pasadena, California 91125

D. Antreasyan,[c] Y. F. Gu,[d] W. Kollman,[e] K. Strauch, K. Wacker,[f]
and A. Weinstein(g)
Lyman Laboratory of Physics, Harvard University, Cambridge, Massachusetts 01238

D. Aschman,[h] M. Cavalli-Sforza,[i] D. Coyne,[i] C. Newman-Holmes,(j)
and H. F. W. Sadrozinski[i]
Physics Department, Princeton University, Princeton, New Jersey 08544

E. Bloom, F. Bulos, R. Chestnut,[k] J. Gaiser,[l] G. Godfrey, C. Kiesling,[m]
W. S. Lockman,[i] M. Oreglia,[n] and D. L. Scharre[o]
Stanford Linear Accelerator Center, Stanford University, Stanford, California 94309

D. Gelphman,[p] R. Hofstadter, R. Horisberger,[c] I. Kirkbride,[q] H. Kolanoski,[r]
K. Königsmann,[c], R. Lee,[a], A. Liberman,[s] J. O'Reilly,[t] A. Osterheld,[u]
B. Pollock,[v] and J. Tompkins[w]
Physics Department and High Energy Physics Laboratory,
Stanford University, Stanford, California 94305

The total cross section for e^+e^- annihilation into hadrons has been measured by the Crystal Ball collaboration at the SLAC storage ring SPEAR, for center-of-mass energies $\sqrt{s}$ from 5.0 to 7.4 GeV. The data show no evidence for new thresholds or resonant structure in this energy range. The average value of R, the radiatively corrected total hadronic cross section divided by the point p-pair cross section, is $3.44 \pm 0.03 \pm 0.18$. Fitting the order-α_s^2 QCD prediction for R to the Crystal Ball data yields a value for the strong interaction coupling constant of $\alpha_s = 0.12 \pm 0.11$ at $\sqrt{s}$ = 6.0 GeV.

Submitted to Physical Review D.

⋆ Work supported in part by the Department of Energy, contracts DE–AC03–76SF00515 (SLAC), DE–AC02–76ER03064 (Harvard), DE–AC03–81ER40050 (CIT) and DE–AC02–76ER03072 (Princeton); by the National Science Foundation, contracts PHY81–07396 (HEPL), PHY79–16461 (Princeton) and PHY75–22980 (CIT); and by the NATO Fellowship (H.K.) and the Chaim Weizmann Fellowship (F.P.).

HADRON PRODUCTION IN e^+e^- ANNIHILATION FROM $\sqrt{s}$ = 5.0 TO 7.4 GeV

C. Edwards,[a] R. Partridge,@) C. Peck, and F. C. Porter
Physics Department, California Institute of Technology, Pasadena, California 91125

D. Antreasyan,[c] Y. F. Gu,[d] W. Kollman,[e] K. Strauch, K. Wacker,[f]
and A. Weinstein(g)
Lyman Laboratory of Physics, Harvard University, Cambridge, Massachusetts 01238

D. Aschman,[h] M. Cavalli-Sforza,[i] D. Coyne,[i] C. Newman-Holmes,(j)
and H. F. W. Sadrozinski[i]
Physics Department, Princeton University, Princeton, New Jersey 08544

E. Bloom, F. Bulos, R. Chestnut,[k] J. Gaiser,[l] G. Godfrey, C. Kiesling,[m]
W. S. Lockman,[i] M. Oreglia,[n] and D. L. Scharre[o]
Stanford Linear Accelerator Center, Stanford University, Stanford, California 94309

D. Gelphman,[p] R. Hofstadter, R. Horisberger,[c] I. Kirkbride,[q] H. Kolanoski,[r]
K. Königsmann,[c], R. Lee,[a], A. Liberman,[s] J. O'Reilly,[t] A. Osterheld,[u]
B. Pollock,[v] and J. Tompkins[w]
Physics Department and High Energy Physics Laboratory,
Stanford University, Stanford, California 94305

The tot al cross section for e^+e^- annihilation into hadrons has been measured by the Crystal Ball collaboration at the SLAC storage ring SPEAR, for center-of-mass energies $\sqrt{s}$ from 5.0 to 7.4 GeV. The data show no evidence for new thresholds or resonant structure in this energy range. The average value of R, the radiatively corrected total hadronic cross section divided by the point p-pair cross section, is $3.44 \pm 0.03 \pm 0.18$. Fitting the order$-\alpha_s^2$ QCD prediction for R to the Crystal Ball data yields a value for the strong interaction coupling constant of a, = 0.12 ± 0.11 at $\sqrt{s}$ = 6.0 GeV.

Pacs number 13.65.+i

Present addresses:

(a) Jet Propulsion Laboratory, Pasadena, CA 91109, USA.

(b) Brown University, Providence, RI 02912, USA.

(c) CERN, EP Division, 1211 Geneva 23, Switzerland.

(d) Institute of High Energy Physics, Academia Sinica, Beijing, People's Republic of China.

(e) Hermann Distel Strasse 28, D-2050 Hamburg 80, Federal Republic of Germany.

(f) III Phys. Inst. der Techn. Hochschule, Aachen, Federal Republic of Germany.

(g) California Institute of Technology, 452-48 Physics, Pasadena, CA 91125, USA.

(h) University of Cape Town, Physics Department, Cape Town, South Africa.

(*i*) Santa Cruz Institute for Particle Physics, University of California, Santa Cruz, CA 95064, USA.

(*j*) Fermi National Accelerator Laboratory, Batavia, IL 60510, USA.

(*k*) 830 Tulane Drive, Mountain View, CA 94040, USA.

(*l*) IntelliCorp, Mountain View, CA 94040, USA.

(m) Max Planck Institute for Physics and Astrophysics, D-8000 Munich 40, Federal Republic of Germany.

(n) Enrico Fermi Institute, University of Chicago, Chicago, IL 60637, USA.

(*o*) Theta Corporation, Mountain View, CA 94041, USA.

(p) Adobe Systems, Incorporated, 1585 Charleston Rd, P. 0. Box 7900, Mountain View, CA 94039, USA.

(q) 911 K. Industrial Way, Lodi, CA 95240, USA.

(r) Universität Dortmund, Dortmund, Federal Republic of Germany.

(s) Schlumberger-Doll Research Center, Ridgefield, CT 06877, USA.

(t) VIDCO Inc., Cupertino, CA 95014, USA.

(u) L59, Lawrence Livermore Laboratory, Livermore, CA 94550, USA.

(v) Digital Applications International, Axtel House, 24 Warwick, London SW1, United Kingdom.

(w) Superconducting Super Collider Laboratory, 2550 Beckleymeade Avenue, Dallas, TX 75237, USA.

I. INTRODUCTION

A fundamental test of the picture that hadron production in e^+e^- collisions proceeds through the formation of a virtual photon which then couples to the charges of a quark-antiquark pair is the measurement of the lowest-order hadronic cross section, σ^0_{had}, divided by the calculated lowest-order p-pair cross section, $\sigma^0_{\mu\mu}$. This ratio, R, is expected to depend only on the dynamics of the coupling of the quark-antiquark pair to the virtual photon.

In the quark-parton model' (QPM), where strong interaction effects among the outgoing quarks are neglected, R is equal to the sum of the squares of the quark charges (Q_i) times a kinematic factor:

$$R_{\mathrm{QPM}} = 3\sum_{i=1}^{n_f}\left(\frac{\beta_i(3-\beta_i^2)}{2}\right)Q_i^2 \quad , \qquad \text{[I.1]}$$

where

$$\beta_i = \left(\frac{s-4m_i^2}{s}\right)^{1/2} \quad , \qquad \text{[I.2]}$$

m_i is the mass^2 of the i^{th} quark, β_i is its velocity relative to the speed of light, $\sqrt{s}$ is the center-of-mass energy of the e^+e^- system, n_f is the number of quark flavors which can be produced, and the factor of 3 accounts for the three different color degrees of freedom. In the energy region of the measurements reported in this paper, n_f = 4, and $R_{\mathrm{QPM}} \approx 3.3$. According to the theory of Quantum Chromodynamics (QCD), the emission of one or more hard gluons in the final state is expected to raise this prediction by about 10%, an increase which is proportional to the value of the running strong coupling constant, a,(s).

Previous measurements[3] of R in the range $5.0 < \sqrt{s} < 7.4$ GeV have indicated a possible discrepancy[4] between theory and experiment. At $\sqrt{s}$ = 7.0 GeV

the data lie about 16% above the theory, while at 5.0 GeV the discrepancy is only 5-8%. The systematic scale error in these data is typically 10–12%. While the apparent disagreement between theory and experiment may be due to systematic problems in the data, Barnett et *al.*[4] have considered the possibility that there may be a threshold for new particles near $\sqrt{s}$ = 6.0 GeV. To resolve these possibilities, the Crystal Ball collaboration undertook a program to measure R with reduced systematic errors. Initially, data were collected at $\sqrt{s}$ values of 5.2, 6.0, 6.5 and 7.0 GeV for a total integrated luminosity of 0.4 pb^{-1}. A second, higher statistics run covered 11 energy points between 5.0 and 7.4 GeV for an integrated luminosity of 3.8 pb^{-1}. These two datasets are henceforth referred to as "Run 1" and "Run 2," respectively. All data reported here were collected at the SLAC e^+e^- storage ring SPEAR.

The experimentally measured value of R is obtained as follows:

$$R = \frac{\sigma^0_{had}}{\sigma^0_{\mu\mu}} = \frac{\sigma^{obs}_{had}}{\sigma^0_{\mu\mu} \cdot \bar{\epsilon}_{had} \cdot (1+\delta)} \quad , \qquad [I.3]$$

$$\sigma^{obs}_{had} = \frac{N_{coll} - N_{bg}}{\mathcal{L}} - (\epsilon\sigma)_{\tau\tau} - (\epsilon\sigma)_{\gamma\gamma} \quad , \qquad [I.4]$$

where σ^{obs}_{had} is the observed hadronic cross section for e^+e^- annihilation into hadrons; $\bar{\epsilon}_{had}$ is the calculated detection efficiency for observing these events. The bar indicates that this efficiency is averaged over all hadronic events, including those with initial-state radiation. The factor $\bar{\epsilon}_{had}$ contains the higher-order Quantum Electrodynamic (QED) corrections which must be applied to σ^0_{had} in order to obtain σ^{obs}_{had}. The quantity N_{coll} is the number of candidate hadronic events recorded during a colliding-beam run with integrated luminosity and selected by appropriate criteria. To obtain σ^{obs}_{had}, the number N_{coll} must be

corrected for backgrounds from beam-gas scattering, τ decays and two-photon collisions. N_{bg} , the number of background beam-gas events, is estimated from separated-beam data collected at each energy. The terms $(\epsilon\sigma)_{\tau\tau}$ and $(\epsilon\sigma)_{\gamma\gamma}$ are the calculated cross sections for detecting events from the background processes

$$e^+e^- \rightarrow \tau^+\tau^-(\gamma) \ , \ \tau^\pm \rightarrow \text{anything} \qquad \text{[I.5]}$$

and

$$e^+e^- \rightarrow e^+e^-\gamma\gamma \ , \qquad \gamma\gamma \rightarrow \text{hadrons} \qquad \text{[I.6]}$$

in the colliding-beam data sample.

In Section II, the properties of the Crystal Ball detector relevant to the *R* measurement are described. In Section III, the procedure to obtain the beam-beam luminosity is presented. Section IV describes the criteria for selecting candidate hadronic events from e^+e^- annihilation. Sections V.l and V.2 describe the procedures used to estimate the backgrounds in the colliding-beam data sample due to beam-gas, r-pair and two-photon collision processes. Section V.3 discusses the calculation of the efficiency $\bar{\epsilon}_{had}$ for observing annihilation hadronic events in the apparatus after event selection criteria have been applied. In Section V.4, the results of the radiative correction procedure described in Appendix A are presented. In Section V.5, the sensitivity of the results to the criteria used to reject beam-gas events is explored. In Section VI. 1, the measured *R* values are presented and compared with results obtained by other experiments in the range $5.0 < \sqrt{s} < 9.4$ GeV. In Section VI.2, the QCD prediction for *R* (henceforth referred to as R_{QCD}) is fitted to the data to extract α_s at $\sqrt{s} = 6.0$ GeV. A comparison is then made with other values of α_s as determined from measurements of *R* in the PEP/PETRA energy range.

II. APPARATUS

The Crystal Ball detector shown in Fig. 1 is a nonmagnetic calorimeter designed to measure electromagnetically showering particles (y, e*) with excellent resolution in energy and angle. The various components of the detector have been described in detail elsewhere[5,6]; the properties especially relevant to this measurement are summarized below.

The main component of the Crystal Ball detector is a transversely segmented shell of 672 thallium-doped sodium iodide [NaI(Tl)] crystals, 16 radiation lengths thick, providing 93% of 47r steradians solid angle coverage for both neutral and charged particles. Under experimental operating conditions, this portion of the detector (henceforth referred to as the "Ball"), achieves a photon energy resolution σ_E/E = $(2.7 \pm 0.2)\%/E^{1/4}$ (E in GeV) and an energy-dependent angular resolution of 1° to 2°. Four auxiliary arrays of NaI located near the, beam pipe extend the solid angle coverage of the main ball to 98% of 4π steradians. Signals from this portion of the apparatus, referred to as the "endcap" crystals, are not used in this analysis. The energy calibration of the NaI(Tl) crystals has been described in detail elsewhere.[5,6]

In addition to the NaI(Tl), a central tracking system of magnetostrictive (MS) and multiwire proportional (MWPC) chambers immediately surrounding the beam pipe provide charged and neutral particle separation over the entire solid angle covered by the Ball.

Two independent triggering systems permit the detection of multihadron events entering the solid angle of the Ball with nearly 100% efficiency. Figure 2 illustrates the geometrical layout of the Crystal Ball detector. The icosahedron,

or 20-sided polygon, forms the basis for the detector's geometry, although the crystals are stacked to form two mechanically separate hemispheres, one above and one below the plane of the SPEAR storage ring. Each face of the icosahedron, or "major triangle," is subdivided into four smaller units, or "minor triangles." In turn, each minor triangle consists of nine optically isolated crystals, also referred to as "modules." Triggers are constructed from the analog sums of signals from the minor triangles, as well as from the central tracking system.[5] Neither the endcap modules nor the first layer of modules surrounding the tunnel region are used in defining the various triggers.

The first triggering system[5] initiates the readout of the apparatus if any of the following conditions are met:

1. *Total* energy *trigger:* The total energy in the Ball exceeds 1100 MeV.

2. *Topology trigger:* At least 150 MeV of deposited energy is required in ≥ 1 major triangles in each of six hemispheres defined by three different planes each containing the beam axis.[7] Although not available during Run 1, this trigger imposes a loose momentum balance requirement perpendicular to the beam direction, allowing the detection of low-mass states produced in $\gamma\gamma$ collisions.[8]

3. *Multiplicity trigger:* In two or three major triangles the deposited energy per major triangle exceeds 140 MeV and signals from the MWPC chamber indicates the presence of a charged track, or the energy in each of four or more major triangles exceeds 140 MeV.

4. *Quark trigger:* In one or more pairs of back-to-back minor triangles, the energy per minor triangle exceeds 40 MeV.

A second, electronically independent system[5] generates triggers if either or both of the following two conditions are satisfied:

1. *NIM total energy* trigger: A total energy trigger similar to the one mentioned above.

2. *NIM topology trigger:* The energy in each of the two mechanically separate hemispheres exceeds 140 MeV and the total energy in the Ball is greater ---than 600 MeV.

Each of the triggers is required to register signals only within a 40-nsec gate centered on the beam-crossing signal. Typically, data are logged at a trigger rate of 3 to 4 hz corresponding to a live time of about 85%.

The most important trigger for this analysis is the total energy trigger. The efficiency of all triggers for detecting hadronic events is included in the overall hadronic event detection efficiency discussed in Section V.3. The overall trigger efficiency is estimated to be greater than 99% for Monte Carlo-simulated hadronic events which pass the selection criteria described in Section IV.

Finally, a precision small-angle luminosity monitor provides a second determination of the beam luminosity which complements the measurement made by the Ball. The design of this device is essentially the same as that used in a previous experiment at SPEAR.' This monitor records Bhabha-scattered electrons and positrons emerging at approximately 4.25' relative to the beam direction. Each scattered particle passes at nearly normal incidence through a 0.03 radiation length thick beam pipe window. Four lead scintillator shower counters, each 12.5 radiation lengths thick, are mounted symmetrically about the interaction region in the plane of the SPEAR storage ring to measure the energy of

the scattered leptons. A fiducial-defining scintillation counter and its associated shower counter, together with the shower counter in the opposite arm, defines a luminosity monitor "arm." The coincidence rates in all four arms are summed together to provide a measure of the Bhabha counting rate which is insensitive to relative transverse and longitudinal displacements between the interaction point and the monitor.[9]

-In summary, the features of the Crystal Ball detector particularly relevant to the *R* measurement are:

1. Its large and uniform acceptance.

2. The calorimetric nature and redundancy of the event triggers which allow hadronic systems to be detected with high efficiency.

3. A precision small-angle luminosity monitor complementing the luminosity measurement in the main Ball.

III. LUMINOSITY

The luminosity of the colliding e^+e^- beams is measured using the QED processes:

$$e^+e^- \rightarrow e^+e^- \quad , \qquad \text{[III.1]}$$

$$e^+e^- \rightarrow \gamma\gamma \quad , \qquad \text{[III.2]}$$

where one or more radiative photons may also be present in each reaction. Two independent methods are used to measure the luminosity. Method 1 measures

the small-angle Bhabha scattering rate (process [III.1]) into precision luminosity counters located around the beam pipe. Method 2 measures the large-angle Bhabha and $\gamma\gamma$ QED rates into the Ball itself. The value of $\mathcal{L}$ is obtained by averaging the results of the two methods. A comparison of the two results provides an estimate of the systematic error. For both methods, the integrated luminosity for a certain period of data taking is given by:

$$\mathcal{L} = \frac{N}{\sigma} \quad , \qquad \text{[III.3]}$$

where N is the number of QED events observed and σ is the QED cross section associated with the small-angle monitor (σ_{small}) or the Ball (σ_{large}).

The small-angle luminosity monitor constant, $s \cdot \sigma_{small}$, is determined by a numerical integration of the radiative Bhabha cross section" over the acceptance of the monitor. The small-angle monitor constant is determined to be:

$$s \cdot \sigma_{small} = 17240 \ (\text{GeV}^2\text{-nb}) \quad . \qquad \text{[III.4]}$$

In the large-angle luminosity measurement, only the energies and directions determined from the electromagnetic shower patterns in the Ball are used to identify QED events. No charged-particle "tag" from the central tracking chambers is required. Thus, there is no systematic uncertainty in the luminosity measurement due to tagging efficiency; both QED processes [III.1] and [III.2] contribute to the large-angle luminosity event sample.

To identify large-angle QED events, each recorded event is analyzed for connected regions[12] of energy. Each connected region of energy in the NaI(Tl) is

scanned for local energy maxima. The module containing the local maximum energy is referred to as the "bump" module. A direction is then associated with that bump, using a modified version of the shower direction algorithm described in Ref. 13 to take into account the vertex position. The shower energy is computed by summing the energy deposited in the bump module with the 12 neighboring crystals. The lateral energy distribution in the 13 crystals is used to correct the summed energy for position-dependent energy losses.[5] A global correction factor of 1.0225[5] is also applied to account for lateral leakage outside of the 13 crystals. This corrected energy sum is henceforth referred to as $E_{\Sigma 13}$.

Events from processes [III.1] and [III.2] are selected by the following QED criteria:

1. At least two showers each with $x_{13} > 0.5$, where $x_{13} = 2 . E_{\Sigma 13}/\sqrt{s}$.
2. For at least two showers satisfying the previous condition, $|\cos\theta_z^s| < 0.75$, where θ_z^s is the angle between the shower direction vector and the beam direction.
3. For at least one pair of showers satisfying the previous two criteria, the smaller of the two angles ϕ_{acop} between the shower vectors projected onto the plane perpendicular to the beam direction must satisfy $160° < \phi_{\text{acop}} < 180°$.

The Berends-Kleiss Monte Carlo event generators[14,15] are used to calculate the observed large-angle cross sections for processes [III.1] and [III.2] at $\sqrt{s}$ = 5.2, 6.0, 6.75 and 7.4 GeV. These generators include order-a radiative corrections to the lowest order processes. The magnitude of the radiative correction is approximately 3% in all cases. The generated Bhabha events are required to have

$|\cos\theta_z^g| < 0.985$ for the e^+ and e^- tracks, where θ_z^g is the angle between the generated Monte Carlo track and the beam direction. In addition, events from either reaction are required to have at least two generated tracks with $|\cos\theta_z^g| < 0.88$ and $E/E_{beam} > 0.1$. For both processes, the product $s \cdot \sigma$ is independent of $\sqrt{s}$.

The longitudinal position of the event vertex is generated by convoluting two Gaussian beam bunches. Each bunch is assumed to have a longitudinal standard deviation σ_{bunch} of 2.5 cm. The size of the luminous region is then $\sigma_{bunch}/\sqrt{2}$, or 1.8 cm. The x- and y-coordinates of the vertex are fixed at zero.[16]

The response of the Ball to the generated events is simulated by passing each sample of events through the *EGS3*[17] Monte Carlo program. Showers are reconstructed in the same manner as for real data and QED criteria (l-3) are applied. At center-of-mass energies of 5.2, 6.0, 6.75 and 7.4 GeV, σ_{large} , defined as the sum of observed cross sections for processes [III.1] and [III.2], is computed. The product $s \cdot \sigma_{large}$ is s-independent and an average of $s \cdot \sigma_{large}$ over the four center-of-mass energies yields

$$s \cdot \sigma_{large} = (1429 \pm 19)\ (\text{GeV}^2\text{-nb}) \quad , \qquad \text{[III.5]}$$

where the error is due to the statistical uncertainty in the detected Monte Carlo event sample.

Figures 3(a) and (b) show, respectively, the $E_{\Sigma 13}$ energy normalized to the beam energy and the cos θ_z distributions for events passing the luminosity event selection criteria. The Monte Carlo distributions (histograms) are normalized to the same luminosity as the data. The energy and angular distributions of the

data are matched well by the Monte Carlo. By varying the cos θ_z^s requirement from 0.8 to 0.6 at $\sqrt{s}$ = 7.4 GeV, the luminosity changes by less than 2%.

Table I summarizes the luminosities measured by the large- and small-angle monitors. The average luminosity $\mathcal{L}$ for each data sample is defined to be the arithmetic average of the large- and small-angle luminosities, where the statistical error is dominated by the large-angle measurement. The errors on $\mathcal{L}_{large}$ are-purely statistical and are obtained by adding the statistical error in σ_{large} ($\pm$ 1.3%), in quadrature with the error in the number of detected large-angle QED events. The first error in $\mathcal{L}$ reflects the statistical error in the large-angle measurement. The second error in $\mathcal{L}$ is the point systematic uncertainty and is taken to be one-half of the difference between the small- and large-angle measurement s.

Figure 4 displays the ratio of the large- to small-angle luminosity for both running periods. The average ratios for Run 1 and Run 2 are (0.977 $\pm$ 0.011) and (0.977 $\pm$ 0.006), respectively, where the errors on these numbers are purely statistical. The largest systematic differences between the large- and small-angle luminosities occurs above 7.0 GeV.

In addition to the statistical and point systematic errors listed above, an overall systematic scale uncertainty on the luminosity measurement is estimated as follows. The systematic scale uncertainty on the large-angle luminosity measurement is estimated by adding in quadrature $\pm$ 2.2% from uncertainties in the Monte Carlo simulation of the apparatus and shape of the vertex distribution and $\pm$ 2.0% based on measuring the variation of the luminosity as a function of cos 8,. The systematic error in the measurement of the small-angle luminosity is

estimated to be $\pm$ 4.0%.[18] The large- and small-angle systematic errors are added in quadrature and divided by two, to obtain a systematic uncertainty on $\mathcal{L}$ of $\pm 2.5\%$. To this number an additional $\pm 0.2\%$ scale error is added linearly to account for higher-order radiative corrections,[19] resulting in a $\pm$ 2.7% systematic scale uncertainty in the determination of the luminosity.

IV. HADRONIC EVENT SELECTION

This section describes the criteria used to isolate e^+e^- annihilation hadronic events from events due to the following background sources:

1. Large-angle Bhabha and $\gamma\gamma$ events.
2. Cosmic-ray muons and QED $\mu\mu$ events.
3. Events from beam-gas and beam-wall scattering and collectively referred to "beam-gas" events.
4. QED production of r-pairs.
5. Events from two-photon collisions.

In addition to hadronic events from e^+e^- annihilation, the raw data sample includes significant contributions from all sources listed above. The hadronic event selection process described below effectively removes all background events from sources 1 and 2. Beam-gas background levels are determined through separated-beam runs at each energy; the last two background levels are estimated by Monte Carlo simulation. For most of the analyses, only the deposited energy patterns in the Ball are used to select events of a given type.

Events are first analyzed for connected regions and bumps, as described in Section III. Hadronic events are then required to satisfy the conditions listed below :

1. *QED cut:* Events are rejected as $e^+e^-(\gamma)$ or $\gamma\gamma(\gamma)$ if more than one shower has $x_{13} > 0.5$, or if any shower has $x_{13} > 0.75$ and there are fewer than four connected regions with at least 50 MeV of deposited energy.

2. *Multiplicity cut:* Hadronic events are required to have at least three connected regions, each with at least 50 MeV of energy. In addition, at least one bump module must be associated with a track in the central tracking chamber.

3. Cosmic-ray *cut:* The time resolution of the sodium iodide's readout electronics is insufficient to effectively reject cosmic-ray events. Instead, cosmic-ray and $\mu\mu\gamma$ events remaining in the data sample after the multiplicity cut are isolated by topological criteria based on the highly collimated, or "jet-like" patterns of energy deposition characteristic of these events. The following quantities, defined below, are used to select these events. An "energy vector" $\vec{E}_k$ associated with the k^{th} crystal is defined to be the product of the deposited energy, E_k, and the unit vector $\hat{n}_k$ pointing to the center of that crystal:

$$\vec{E}_k = E_k \hat{n}_k = (E_k^x, E_k^y, E_k^z) \quad . \qquad \text{[IV.1]}$$

An "energy tensor" $T^{\alpha\beta}$ is defined as

$$T^{\alpha\beta} = \sum_k \delta^{\alpha\beta} \vec{E}_k^2 - E_k^\alpha E_k^\beta \quad , \qquad \text{[IV.2]}$$

where the indices α and β refer to the three spatial components of $\vec{E}_k$. The smallest eigenvalue of $T^{\alpha\beta}$ is

$$P^2_{t\text{-}jet} = \sum_k \vec{E}_k^2 - (\vec{E}_k \cdot \hat{\xi})^2 \quad , \qquad \text{[IV.3]}$$

where $\hat{\xi}$ is the unit vector parallel to the direction of the cosmic ray. $P^2_{t\text{-}jet}$ is the sum of the squares of the energy vector components perpendicular to the direction of the cosmic ray. Candidate hadronic events are required to satisfy

$$A \equiv \frac{\left|\sum_k \vec{E}_k\right|}{\sum_k E_k} \leq \frac{\log_{10}(P^2_{t\text{-}jet}/\mathrm{GeV}^2) + 2.8}{1.8} \quad , \qquad \text{[IV.4]}$$

where A is the energy-weighted asymmetry. $P^2_{t\text{-}jet}$ is required to be larger for events with larger energy asymmetries.

4. Beam-gas *cut:* The following requirement removes events with low transverse momentum relative to the beam direction and is more stringent at higher center-of-mass energies and for events with larger energy asymmetries or smaller visible energies. Hadronic events are required to satisfy the following condition:

$$\eta(x_{vis}, P^2_{t-z}, s) \equiv \log_{10}(P^2_{t-z}/\mathrm{GeV}^2) - (\eta_1(s) + A \cdot \eta_2(x_{vis})) > 0 \quad , \quad \text{[IV.5]}$$

where the quantities x_{vis} , the visible energy in the Ball divided by the center-of-mass energy, and P^2_{t-z} , the sum of the squares of the energy vector components perpendicular to the beam direction, are defined as

$$x_{vis} \equiv \frac{\sum_k E_k}{\sqrt{s}} \qquad \text{[IV.6]}$$

$$P_{t-z}^2 \equiv \sum_k \vec{E}_k^2 - (E_k^z)^2 \quad . \qquad \text{[IV.7]}$$

The η_1 and η_2 functions are given by

$$\eta_1 = -1.0 + 0.1 \cdot (\sqrt{s}/\text{GeV} - 7.0) \; ; \qquad \text{[IV.8]}$$

$$\eta_2 = 0.6 \qquad \text{if } x_{vis} < 0.25 \; ; \qquad \text{[IV.9]}$$

$$= 2.4 \cdot (0.5 - x_{vis}) \qquad \text{if } 0.25 < x_{vis} < 0.5 \; ; \qquad \text{[IV.10]}$$

$$= 0.0 \qquad \text{if } x_{vis} > 0.5 \; . \qquad \text{[IV.11]}$$

Separated-beam data are then used to subtract the residual beam-gas contamination from the hadronic event sample (cf. Section V.1).

5. *Asymmetry cuts:* The left-right, top-bottom, and front-back hemisphere asymmetries are defined as follows:

$$A_{left-right} \equiv \frac{\left| \sum\limits_{\substack{k \\ E_k^x>0}} |\vec{E}_k| - \sum\limits_{\substack{k \\ E_k^x<0}} |\vec{E}_k| \right|}{\sum_k E_k} \quad , \qquad \text{[IV.12]}$$

$$A_{top-bottom} \equiv \frac{\left| \sum\limits_{\substack{k \\ E_k^y>0}} |\vec{E}_k| - \sum\limits_{\substack{k \\ E_k^y<0}} |\vec{E}_k| \right|}{\sum_k E_k} \quad , \qquad \text{[IV.13]}$$

$$A_{front-back} \equiv \frac{\left| \sum\limits_{\substack{k \\ E_k^z>0}} |\vec{E}_k| - \sum\limits_{\substack{k \\ E_k^z<0}} |\vec{E}_k| \right|}{\sum_k E_k} \quad . \qquad \text{[IV.14]}$$

Hadronic events are required to satisfy the following three conditions:

$$A_{left-right} < 0.8 \; , \qquad \text{[IV.15]}$$

$$A_{top-bottom} < 0.8 \; , \qquad \text{[IV.16]}$$

$$A_{front-back} < 0.8 \ . \qquad \text{[IV.17]}$$

These requirements are designed to remove events from beam-gas interactions, $\gamma\gamma$ collisions and large missing energy τ decays which pass the previous requirements.

Figure 5 illustrates the requirement used to isolate hadronic events from cosmic rays. The correlation between A and $P^2_{t\text{-}jet}$ for cosmic-ray data[20] is shown in Fig. 5(a). Cosmic rays passing through the center of the detector produce events with small A and small $P^2_{t\text{-}jet}$; those grazing the Ball produce events with larger A and larger $P^2_{t\text{-}jet}$. The solid curve is defined by the equality in Eq. [IV.4]; events to the left of the solid curve are removed from the hadronic sample. For comparison, Monte Carlo hadronic events are generated at $\sqrt{s}$ = 5.0 GeV, using the Lund Monte Carlo program *JETSET* 4.3, henceforth referred to as LUND 4.3.[21,22] As indicated in Fig. 5(b), fewer than 4% of the reconstructed hadronic events are removed by the cosmic-ray requirement.

The timing of the energy deposition in the sodium iodide relative to the beam crossing is used to estimate the contamination due to cosmic rays. Figure 6 shows the timing in nanoseconds of the energy deposition in the sodium iodide relative to the beam-crossing signal for different levels of event selection. The lower and upper time limits of each plot are defined by the 40-nsec timing gate in the experiment. The timing distribution from the raw event sample with only Bhabha and $\gamma\gamma$ QED events removed is shown as the upper histogram in Fig. 6. The flat background of events are due to cosmic rays which comprise about 30% of the total entries in this plot. Imposing the multiplicity requirement and condition [IV.4] reduces the cosmic-ray background to less than 2% of the

remaining events, as shown in the middle histogram in this figure. Finally, the lower histogram shows the timing distribution for events passing all hadronic selection requirements. As seen from this figure, the background from out-of-time events comprises about 1% of this sample. This small background is removed by the subtraction procedure described in Section V.l.

The level of QED p-pair events in the final hadronic sample is estimated using the Berends-Kleiss $e^+e^- \rightarrow \mu\mu\gamma$ Monte Carlo event generator.[23] At $\sqrt{s}$ = 7.4 GeV, radiative p-pair events contribute a background of less than *0.7%* to the observed hadronic event sample. This background is neglected in the remainder of this analysis.

The most serious sources of background in the hadronic data sample are due to beam-gas and beam-wall interactions. Due to the limited tracking capability of the central detector, beam-gas events cannot be removed efficiently by making stringent requirements on the position of the event vertex. Instead, the beam-gas and asymmetry requirements described previously are imposed.

At $\sqrt{s}$ = 7.0 GeV, Fig. 7shows the distribution of the beam-gas v-function for hadronic events generated by *LUND* 4.3 and for recorded separated-beam events. The events in both distributions have already passed the QED and cosmic-ray requirements. The normalization of the separated-beam data is discussed in Section V.l. The Monte Carlo sample size is the same as that of the data. Beam-gas events in this plot having negative η are clearly separated from the bulk of the hadronic events having positive η values.

Figure 8(a) displays the visible energy fraction x_{vis} deposited in the Ball at $\sqrt{s}$ = 7.0 GeV, for all triggered events. This plot is dominated by the large

number of beam-gas and $\gamma\gamma$ collision events at low x_{vis}, and to showering QED events at large x_{vis}. Only about 2.5% of the events in Fig. 8(a) correspond to real hadronic events. Figure 8(b) shows the x_{vis} distribution in the Ball for events passing all the hadronic event selection criteria. The backgrounds present in the initial data sample have been nearly eliminated in the final data sample. The remaining background sample, depicted by the shaded histogram, is estimated and statistically subtracted, as described in Section V.l.

The solid curve in Fig. 8(b) is a fit to the hadronic event detection efficiency estimated by *LUND* 4.3. The efficiency loss at low and high x_{vis} is due to the criteria which are designed to remove the beam-gas, $\gamma\gamma$ collision and radiative QED events. As can be seen from this curve, hadronic events with visible energy fractions as low at 0.15 are detectable.

V. CORRECTIONS

Table II shows N_{coll}, the number of colliding beam events passing the hadron selection criteria outlined in Section IV for each data sample at a given value of $\sqrt{s}$ in Runs 1 and 2. Each sample still includes background events from three sources:

1. N_{bg} events from beam-gas and beam-wall interactions.

2. $N_{\tau\tau}$ events from $\tau-$pair production by e^+e^- annihilation (Eq. [I.5]).

3. $N_{\gamma\gamma}$ events from two-photon collisions (reaction [I.6]).

To obtain the corresponding values of R (Eqs. [I.3]–[I.4]), the beam-gas background, N_{bg}, is first statistically subtracted from N_{coll}, as described in Sec-

tion V.l. The observed cross sections for the remaining backgrounds are estimated by Monte Carlo simulation and subtracted from the quantity $(N_{coll} - N_{bg})/\mathcal{L}$ to obtain the observed hadronic cross section, σ_{had}^{obs}. Through the factor $\bar{\epsilon}_{had} \cdot (1 + \delta)$, σ_{had}^{obs} is corrected for acceptance and event selection losses and for initial state radiation to obtain σ_{had}^{0}. This quantity is then divided by the calculated lowest-order p-pair cross section to obtain R.

-T-he efficiency factors appearing in Eqs. [I.3] and [I.4] are estimated by Monte Carlo simulation. This process involves the generation of track four-vectors and event vertices. The response of the detector to these tracks is then simulated. Finally, events are passed through the same event reconstruction and data analysis programs as are used to analyze real data.

Tables II and III list for each data sample in Runs 1 and 2 the contributions of these three background sources in terms of percentage of N_{coll}. The following sections describe how these background estimates are obtained.

V.l Beam-Gas Background Subtraction

The hadronic event selection criteria are applied to the separated-beam data and at each energy, the number of separated beam events N_{sep} surviving these criteria are obtained. The number of beam-gas events N_{bg} in the corresponding hadronic event sample is given by:

$$N_{bg} = f \cdot N_{sep} \quad , \qquad [V.1]$$

where the constant of proportionality, f, is determined by independent methods.

In the first method, the product of storage ring pressure times beam current for each beam integrated over time (PCT) is measured for both colliding- and separated-beam running. The PCT information was available only during Run 2. From this method, the normalization constant, f_{PCT}, is simply the ratio:

$$f_{\mathrm{PCT}} = \frac{\mathrm{PCT}_{coll}}{\mathrm{PCT}_{sep}} \quad . \qquad [V.2]$$

For--Run 1, no storage ring vacuum information was available. Instead, the normalization constant is determined from the ratio of colliding- to separated-beam current integrals, $\int Idt$.

In the second method, samples of events which fail the beam-gas rejection requirement, Eq. [IV.5], but which pass all other hadronic event criteria are used to determine the normalization between the colliding- and separated-beam data. The quantities bg_{sep} and bg_{coll} are the numbers of events occupying the beam-gas enriched portions of the separated- and colliding-beam data samples, respectively. The numbers of r-pair- and $\gamma\gamma$ collision events contained in bg_{coll}, denoted as $bg_{\tau\tau}$ and $bg_{\gamma\gamma}$, respectively, are estimated by Monte Carlo simulation (cf. Section V.2). The number of hadronic events from e^+e^- annihilation in the beam-gas enriched colliding beam sample, bg_{hadron}, is estimated by the Monte Carlo simulation described in Section V.3. The normalization constant determined by this method is given by:

$$f_{data} = \frac{bg^*_{coll}}{bg_{sep}} \quad , \qquad [V.3]$$

where

$$bg^*_{coll} = bg_{coll} - bg_{\gamma\gamma} - bg_{\tau\tau} - bg_{hadron} \quad . \qquad [V.4]$$

Typically, $bg_{\gamma\gamma}$, $bg_{\tau\tau}$, and bg_{hadron} comprise 4%, 1%, and 1% respectively, of bg_{coll}. The values obtained for f_{data} are not sensitive to the selection criteria used to define the beam-gas samples.

Shown in Table II are the values of f, the arithmetic mean of the constants f_{PCT} or $f_{\int Idt}$ and f_{data}. These values of f are used to compute N_{bg}, the expected number of beam-gas events in each hadronic event sample, using the observed number N_{sep} of beam-gas events measured during the separated beam running and shown in Table II. The point systematic error in f is estimated to be one-half the difference between f_{data} and $f_{\int Idt}$ (Run 1) or f_{data} and f_{PCT} (Run 2). This error is then propagated through Eqs. [I.3] and [I.4] to compute the point systematic error in R due to the beam-gas subtraction.

The **percentage values of** N_{bg}/N_{coll} are shown in Table II. During Run 1, the background levels ranges from 6% to 15%. In Run 2, the beam-gas contamination varies from 8% to 12% except at $\sqrt{s}$ = 7.4 GeV, where the background level is nearly 18%.

As can be seen from Table III, the relative agreement between the two determinations of the normalization constant is usually better than $\pm 10\%$. However, systematic differences between colliding- and separated-beam running conditions may exist which are not accounted for in f. For example, f_{PCT}, which depends only on the storage ring pressure and beam currents, will not reflect changes in background rates due to systematic differences between colliding and separated beam orbits. The quantity f_{data} is expected to track such differences.

To estimate the systematic error in f due to different colliding- and separated-beam operating conditions, the ratio of normalization constants f/f_{data} is exam-

ined. The average value for this quantity in Run 1 and Run 2 is 1.05 and 0.95, respectively. Based on these estimates of systematic differences between colliding- and separated beam running, we conservatively estimate an overall 10% uncertainty on f. When propagated through Eqs. [I.3] and [I.4], the error in f results in a $\pm 2.2\%$ uncertainty in R.

The remaining significant backgrounds to hadronic events in the colliding-beam sample arise from processes [I.5] and [I.6]. Monte Carlo estimates of the observed cross sections are made for each process, as discussed below.

V.2 T-Pair and Two-Photon Background Subtraction

To estimate the observed cross section for radiative r-pairs, the Berends–Kleiss Monte Carlo program[24] is used to generate radiative r-pair four-vectors. The matrix elements used for the various decay modes of the τ are described in Ref. 25; the branching ratios used in the Monte Carlo simulation are obtained from Ref. 26.

Figure 9 shows the produced and observed radiative r-pair cross sections. The fraction of τ events surviving the hadronic event selection criteria is 30–36%, depending on the center-of-mass energy. The percentage values of $N_{\tau\tau}/N_{coll}$ where $N_{\tau\tau} = \mathcal{L}(\epsilon\sigma)_{\tau\tau}$ are shown for each energy in Table III. The overall magnitude of the r-subtraction is about 8–10%.

The major systematic uncertainty in $(\epsilon\sigma)_{\tau\tau}$ is due to the modeling of missing τ decay modes. Approximately 92% of all τ decays have been accounted for in exclusive decay channels. The unobserved exclusive decays are assumed to proceed through the following modes:

$$\tau^{\pm} \rightarrow \pi^{\pm} 3\pi^0 \nu_\tau \quad ,$$
$$\rightarrow \pi^{\pm} 4\pi^0 \nu_\tau \quad , \qquad [V.5]$$
$$\rightarrow \pi^{\pm} 2\pi^- 2\pi^+ \nu_\tau \quad ,$$

with branching ratios of 2.0%, 2.8% and 2.8%, **respectively. Approximately** 13% of the Monte Carlo τ decays surviving the hadronic event selection criteria come from these modes. Assuming the τ detection efficiency is uncertain by 10% due to the modeling of the missing decay modes leads to a relative uncertainty in R of $\pm$ 1.0%. The relative uncertainty in $(\epsilon\sigma)_{\tau\tau}$ due to the Monte Carlo model for τ production is estimated to be $\pm$ 5%, leading to a relative uncertainty in R of $\pm$ 0.5%. Scaling the $\pm$ 2% systematic error in the detection efficiency of hadronic events (cf. Section V.3) by the ratio $\sqrt{\epsilon_{\tau\tau} \cdot (1 - \epsilon_{\tau\tau})/(\bar{\epsilon}_{had} \cdot (1 - \bar{\epsilon}_{had}))}$ leads to an absolute systematic error of $\sim \pm$ 3.0% in the τ detection efficiency due to uncertainties in the modeling of the detector.- Propagating this error through Eqs. [I.3] and [I.4] leads to a $\pm$ 0.3% relative uncertainty in R. Combining these errors in quadrature, the total systematic error in R due to the τ subtraction is estimated to be $\pm$ 1.2%.

To study the hadronic background due to two-photon collisions, a Monte Carlo model written by D. Burke and L. Golding[27] based on the Equivalent Photon Approximation[28] is used to generate events. In this model, the two-photon collision cross section $\sigma_{\gamma\gamma}$ is given by

$$\sigma_{\gamma\gamma} = \left(\frac{\alpha^2}{\pi}\right) \int_{W^2_{min}}^{s} dW^2 \; F(W^2, s) \sigma^T_{\gamma\gamma}(W^2) \quad , \qquad [V.6]$$

$$\sigma^T_{\gamma\gamma}(\text{nb}) = 300 + 800/W \text{ (GeV)} \quad , \qquad [V.7]$$

where $F(W^2, s)$ is the photon flux factor, W is the available energy in the $\gamma\gamma$ center of mass, and $\sigma^T_{\gamma\gamma}(W^2)$ is the transverse photon-photon cross section for hadron production evaluated in the limit $q^2 \rightarrow 0$. W_{min} is set to 1.0 GeV. The expression for $\sigma^T_{\gamma\gamma}$ in Eq. [V.7] is consistent with the results reported in Ref. 29 and Ref. 30.

In the Monte Carlo model, all particles in the final state are assumed to be pions, and π^+, π^- and π^0 are produced with the same probability. The track momenta are generated according to a limited transverse momentum phase space distribution about the $\gamma\gamma$ direction in the hadron center-of-mass system. The transverse momentum spectrum for each track is modeled by a single Gaussian distribution. The average transverse momentum per track is chosen to be 0.5 GeV. A Poisson distribution with a mean-value of $2.1 + 1.6 \cdot \log(W/\text{GeV})$ is used to describe the total particle multiplicity. Figure 9 shows the resulting values of $\sigma_{\gamma\gamma}$ and $(\epsilon\sigma)_{\gamma\gamma}$. Approximately 10% of the hadronic events from process [III.2] survive after the hadronic selection criteria have been applied. The percentage values of $N_{\gamma\gamma}/N_{coll}$ where $N_{\gamma\gamma} = \mathcal{L}(\epsilon\sigma)_{\gamma\gamma}$ are shown for each energy in Table III. The background of two-photon events in the final hadron sample is 2% to 4%.

The systematic scale error in R from the two-photon background subtraction is estimated to be $\pm$ 1.0%. This error is primarily due to uncertainties in the modeling of the production of hadrons emanating from the two-photon interaction and in the overall magnitude of the two-photon cross section into hadrons.

V.3 Hadronic Event Detection Efficiency

The term $\bar{\epsilon}_{had}$ is the fraction of produced hadronic events which are reconstructed and which satisfy the event selection criteria described in Section IV. Monte Carlo calculations are used to estimate $\bar{\epsilon}_{had}$. The production of quark and gluon jets and their subsequent fragmentation into hadrons is simulated by *LUND 4.3.* Baryons are built up from quark-antidiquark systems, where an ant&quark consists of two quarks in a color anti-triplet state.[31] The standard parameter values of this model are used, with two exceptions:

1. A somewhat harder charmed-quark fragmentation function, derived from D-meson spectra and di-muon production in νN interactions[32] is used.
2. The probability to produce a diquark is taken to be 6.5%, as suggested by SPEAR data,[33] rather than 7.5%.

As shown below, this model reproduces the global features of the data (e.g., visible energy, multiplicity and sphericity[34]) over a wide energy range with a relatively small set of G-independent parameters. This model is described in detail in Ref. 21.

The simulation of a hadronic event in the detector proceeds as follows. First, the center-of-mass energy is degraded by the emission of a photon from either the e^+ or e^- in the initial state. The hadronic event is generated in the rest frame of the virtual photon formed from the e^+e^- annihilation, and then transformed to the laboratory frame. The event vertex is generated from a Gaussian distribution (a = 1.8 cm) in z. The transverse coordinates of the vertex are fixed at $x = y = 0$. Next, the event is passed through a program which simulates the response of the Crystal Ball detector to hadronic and electromagnetically inter-

acting particles. Muon, charged pion, proton and neutron energy depositions in the Ball are simulated by the High Energy Tracking Code (HETC) package.[35] The energy loss (dE/dX) of charged kaons is scaled to the pion dE/dX at the same velocity and the pion and kaon interaction probabilities at fixed kinetic energy are assumed to be equal. K_L^0 and K_S^0 which do not decay in the apparatus are assumed to interact like neutrons with the same velocity. In this simulation, antibaryons are assumed to interact like baryons.

$\bar{\epsilon}_{had}$ is calculated at six different values of $\sqrt{s}$ between 5.0 and 7.4 GeV. The results are shown in Fig. 10(a). The indicated error bars reflect the Monte Carlo statistics. The slight drop in the efficiency at high energies is primarily due to the more stringent beam-gas selection criteria made at these energies. In the version of the detector simulation portion of the Monte Carlo program that is used to calculate the hadronic, r-pair and two-photon event detection efficiencies, all of the acceptance losses present in the real detector are taken into account except the 4-mm gap between the two hemispheres of the Ball and the interstities between the crystals. These effects are included in an updated detector simulation algorithm which is used to compute the Bhabha and QED $\gamma\gamma$ efficiencies in the large-angle luminosity calculation. At $\sqrt{s}$ = 7.0 GeV, the detection efficiency decreases from $\sim$ 87% to $\sim$ 85% when the newer algorithm is used. Altogether, we conservatively estimate that uncertainties in modeling the detector results in a $\pm$ 1.5% uncertainty in $\bar{\epsilon}_{had}$.

Despite the approximations made in the detector response simulation, the global features of the data are reasonably reproduced by the Monte Carlo model over the entire energy range of this measurement. For example, Fig. 11 com-

pares the background subtracted distributions of x_{vis}, sphericity and the bump multiplicity at $\sqrt{s}$ = 5.5 and $\sqrt{s}$ = 7.0 GeV with various predictions of the Lund Monte Carlo model. In the standard version of *LUND* 4.3, an equal mixture of vector *(V)* and pseudoscalar (P) mesons in the quark fragmentation process is assumed. The distributions most sensitive to the vector to pseudoscalar particle ratio are the sphericity and bumps multiplicity distributions. The data favor the standard parameterization of equal parts of P and V. The x_{vis} distributions show little variation in shape from 5.0 GeV [Fig. 11(a)] to 7.4 GeV [Fig. 11(d)], and these distributions are modeled well by *LUND* 4.3. In Fig. 11(b) and (e), the sphericity distributions obtained at $\sqrt{s}$ = 5.0 and 7.0 GeV, respectively, are shown. The shapes of the sphericity distributions are adequately reproduced by *LUND* 4.3 in this energy range, as are the bump multiplicity distributions, shown in Fig. 11(c) and (f), respectively.

The $P^2_{t\text{-}jet}$, P^2_{t-z} and energy asymmetry distributions from the kun 2 data at $\sqrt{s}$ = 7.0 GeV are compared to those generated by *LUND 4.3* in Fig. 12(a–c), respectively. No single value of the vector to pseudoscalar particle ratio is able to completely reproduce the data, although the $P = V$ parameterization yields the best results. At $\sqrt{s} = 7.0$ GeV, the $P = V$, $V = 0$ and $P = 0$ parameterizations result in hadron detection efficiencies $\bar{\epsilon}_{had}$ of $(86.8 \pm 1.0)\%$, $(81.3 \pm 0.9)\%$, and $(90.4 \pm 0.8)\%$, respectively. While these changes in efficiency are large ($\pm 5\%$), the $P = 0$ and $V = 0$ parameterizations of *LUND* 4.3 constitute rather unlikely choices for the vector to pseudoscalar particle ratio, as can be seen by the comparisons in Figs. 11 and 12. Based on the comparison of data and Monte Carlo distributions for these extreme values of P and V, we estimate a $\pm 3\%$ uncertainty in R due to the choice of parameters used in the Lund model.

To check the model dependence of the efficiency estimate further, the Lund model is compared with a second, independent model which does not produce charmed particles or baryons. In this second model, events are generated according to a limited transverse momentum phase space distribution about a jet-axis whose angular distribution with respect to the beam direction is $(1 + \cos^2(\theta_z))$. The parameters in the model are adjusted so that the modeled P^2_{t-z} distribution matches that of the data. The multiplicity distribution predicted by this second model is much broader than that which is seen in the data. Despite its shortcomings, the efficiency estimated by this model agrees with the *LUND 4.3* calculation within the statistical errors of both calculations $(\pm 0.8\%)$. We conclude that the uncertainty in R due to the hadronic model is $\approx \pm 3.0\%$. This result is cross-checked by observing the systematic changes in R due to variations in the beam-gas selection requirement, as described in Section V.5. Our estimate of the $\pm 3.3\%$ uncertainty in R due to the hadronic detection efficiency is obtained by adding the $\pm 3.0\%$ modeling uncertainty in quadrature with the estimated $\pm 1.5\%$ systematic uncertainty due to the detector model.

V.4 Initial State Radiative Corrections

From the results presented in Tables II and III, the observed hadronic cross section σ^{obs}_{had} can be evaluated. To obtain the leading order $[O(\alpha^2)]$ cross section σ^0_{had} corresponding to the diagram in Fig. 13(a), terms containing additional powers of the electromagnetic coupling constant a must be estimated and removed from σ^{obs}_{had}. These higher-order terms, generically referred to as radiative corrections, are represented by a factor $(1 + \delta)$ which multiplies σ^0_{had} to yield the

observed cross section

$$\sigma_{had}^{obs} = \sigma_{had}^{0} \cdot \bar{\epsilon}_{had} \cdot (1+\delta) \quad . \qquad [V.8]$$

In this analysis, the factor δ is approximated as a sum of order-o terms due to the initial state vertex correction diagram, Fig. 13(b), modifications to the virtual photon propagator from e, μ, τ and hadronic vacuum polarization loops, Fig. 13(c), and to bremsstrahlung radiation from one of the initial state charged particles, Fig. 13(d). These corrections are written as δ_{vert} , δ_{vac}^{e} , δ_{vac}^{μ} , δ_{vac}^{τ} , δ_{vac}^{had} , and δ_{γ} , respectively. The vertex correction, vacuum-polarization, and bremsstrahlung diagrams are shown in Fig. 13(b), (c), and (d), respectively. A detailed description of the radiative correction procedure is presented in Appendix A.

The hadronic vacuum polarization and bremsstrahlung correction factors require a model of $\sigma_{had}^{0}(s')$ at other energies s'. To evaluate the effect of this model dependence on R, two different parameterizations of $\sigma_{had}^{0}(s')$ are used to compute $\bar{\epsilon}_{had}$. (1 + δ). The result is shown in Fig. 10(c), where the dashed curve corresponds to a l/s' parameterization of $\sigma_{had}^{0}(s')$ in δ_{γ} , together with a calculation of the hadronic vacuum polarization obtained from Ref. 39. The second parameterization of σ_{had}^{0}(s), referred to as the resonance parameterization, is obtained from the smoothed R-distribution in Fig. 14. A contribution from the narrow vector resonances is also included. The radiative corrections are applied using the resonance parameterization. The l/s' parameterization results in lower average efficiencies and larger radiative corrections than in the resonance parameterization. The product $\bar{\epsilon}_{had}$. (1 + δ) is found to be remarkably insensitive to

the form chosen for $\sigma^0_{had}(s')$, as demonstrated in Fig. 10(c). By comparing the two results for $\bar{\epsilon}_{had} \cdot (1+\delta)$, we conservatively estimate a $\pm 0.5\%$ uncertainty in R due to the modeling of $\sigma^0_{had}(s')$.

The efficiency $\epsilon(k)$ for detecting hadronic events as a function of the radiative photon energy k (expressed as a fraction of the beam energy) is shown in Fig. 15, normalized to the efficiency $\epsilon(0)$ for detecting a nonradiative event. The efficiency to detect an event containing a high energy photon vanishes as $k \to 1$. T-hese events will be highly asymmetric and are removed by the beam-gas and asymmetry requirements described earlier. As described in Appendix A, the radiative corrections will increase sharply as the maximum photon energy fraction approaches 1. Fortunately, this effect is compensated for by the rapidly falling efficiency, which produces a natural cutoff to the bremsstrahlung integral at $k \approx 0.95$. To avoid the uncertainties associated with parameterizing $\sigma^0_{had}(s')$ in the region near the p, ω and ϕ, we impose a maximum photon energy fraction cutoff $k_{max} = 1 - (1\ \mathrm{GeV}^2)/s$ in the Monte Carlo. Lowering the cutoff to 0.8 changes $\bar{\epsilon}_{had} \cdot (1+\delta)$ by less than 0.5%. We therefore estimate a systematic uncertainty on R of $\pm 0.5\%$ due to the choice of k_{max}.

The radiative corrections are approximated by order-o corrections to the initial state. Final state radiative corrections are expected to be small by virtue of the Lee-Nauenberg theorem.[36] This theorem states that there are no leading-log factors contributing to the final state correction when a sum over *all* degenerate states is carried out (since the storage ring picks out a specific energy, the leading-log cancellations do not occur in the initial state). Hence, to lowest order in α, the correction for final state radiation is expected to be $1 + \alpha/\pi$, or 0.23%. We

do not apply this small correction because the effect of final state radiation on the determination of $\bar{\epsilon}_{had}$ is not known. Instead, a systematic error of $\pm 0.25\%$ is assigned to R to account for the estimated uncertainty in the magnitude of final state radiation.

The magnitude of the higher-order corrections is estimated using renormalization group techniques to compute $(1 + \delta)$ to all orders in the leading-log approximation.[37,38] Using the resonance parameterization for $\sigma^0_{had}(s')$ as described in Appendix A, a full leading-log calculation of $(1 + \delta)$ is performed and the result is compared to the analogous order-o calculation, as shown in Fig. 10(b). The difference between the two methods is typically $\sim$ 1%. Since the effect of neglecting higher-order terms on the product $\bar{\epsilon}_{had} \cdot (1 + \delta)$ is not known, we estimate a $\pm 1.0\%$ error in R due to higher-order radiative corrections.

The overall systematic error in R due to -radiative corrections is obtained by adding in quadrature the following uncertainties: $\pm 1.0\%$ from higher-order radiative corrections; $\pm 0.5\%$ from the modeling of σ^0_{had}; $\pm 0.5\%$ for the choice of $k_{\max}$ and $\pm 0.25\%$ from final state radiation, resulting in a total systematic error in R of $\pm 1.3\%$ due to the radiative corrections.

V.5 Sensitivity to Hadronic Selection Criteria.

In order to determine the sensitivity of the final R values to changes in the hadronic selection requirements, new η_1 (s)-functions,

$$\eta_{1-soft} = \eta_1(s) - 0.3 \qquad \text{[V.9]}$$

and

$$\eta_{1-\text{hard}} = \eta_1(s) + 0.3 \qquad \text{[V.10]}$$

are employed in the beam-gas v-function (Eq. [IV.8]) in order to drastically change N_{coll} , $\bar{\epsilon}_{had} \cdot (1 + \delta)$, and the levels of the beam-gas backgrounds in the colliding-beam data samples. Conditions [V.9] and [V.10] are referred to as the "soft" and "hard" beam-gas selection criteria, respectively. The beam-gas background-levels in the $\sqrt{s}$ = 7.4 GeV colliding beam sample corresponding to the hard, standard and soft beam-gas criteria are 8%, 18% and 46%, respectively. The corresponding values for $\bar{\epsilon}_{had} \cdot (1 + \delta)$ are 0.92, 1.06 and 1.10, respectively. The sum of the τ and $\gamma\gamma$ collision background levels remains nearly constant at approximately 12%. Varying the $\eta_1(s)$ function changes the value of the beam-gas normalization constant f_{data} by less than 0.3%.

The R-values resulting from these different selection criteria are shown in Table V, where R_{soft} and R_{hard} are calculated using equations [V.9] and [V.10], respectively. Despite the large changes in the background levels and hadron detection efficiencies due to the different selection requirements, the R-values change only by an average of $\pm$ 3%. However, the R-values obtained from the hard selection criteria are systematically lower than those resulting from the application of the soft beam-gas criteria. Figure 11 shows the background-subtracted distributions of x_{vis} , sphericity and multiplicity of bump modules at $\sqrt{s}$ = 5.0 and 7.0 GeV. Beam-gas events, characterized by small values of these quantities, appear to be properly subtracted at both energies. The same distributions have been examined for the soft and hard beam-gas selection criteria and also show no evidence for under- or over-subtraction.

The P^2_{t-z}-distribution for the standard choice of *LUND* 4.3 parameters at $\sqrt{s}$ = 7.0 GeV is shown as a solid curve in Fig. 12(b). In comparison with the data, the Monte Carlo model appears to under-populate the low-P^2_{t-z} region of this figure. We therefore conclude that the $\pm 3.0\%$ variation in R seen while changing the P^2_{t-z} requirement over a rather large range is due to systematic uncertainties in the determination of $\bar{\epsilon}_{had}$. The results of this analysis are consistent with the previous estimates of the systematic error in R of $\pm 3.3\%$ due to the uncertainties in estimating $\bar{\epsilon}_{had}$.

VI. RESULTS

VI.1 Measured R-Values

The data and calculations presented in Sections III-V have been inserted into Eqs. [I.3] and [I.4] to calculate R at each center-of-mass energy. The results from Run 1 and Run 2 are listed in Table VI and shown in Fig. 16. The error in R consists of three parts: a statistical error δR_{stat}, a point systematic error $\delta R_{point\ sys}$ that depends upon $\sqrt{s}$, and a relative systematic scale error of $\pm 5.2\%$ that is applicable to both data sets. The statistical error is due to the event statistics of the colliding- and separated-beam data. The point systematic error includes the uncertainties in the normalization of the background samples and the statistical errors in the Monte Carlo calculations. These two types of errors are shown in Table VI for each measurement of *R*. The average R-values are obtained by weighting each point with the inverse square of the statistical error. The systematic scale error is obtained by adding in quadrature the various sources listed in Table IV.

Figure 16 shows a comparison of the Crystal Ball results with other experiments.[3,40–44] The Crystal Ball results show no evidence for structure or new thresholds above the QCD continuum, at least at the level suggested by the MARK I data.[4] The average R-value of the Run 1 and Run 2 measurements is:

$$R = 3.44 \pm 0.03 \pm 0.18 \quad , \qquad \text{[VI.1]}$$

where the first error is obtained by adding the statistical and point systematic errors in quadrature and the second error is the systematic scale uncertainty of ±5.2%. This measurement is in good agreement those obtained by the LENA[41] and Crystal Ball[44] experiments in the range $7.4 < \sqrt{s} < 9.4$ GeV (cf. Fig. 16).

VI.2 Comparison with Theory

Using Quantum Chromodynamics (QCD) to calculate the effect of the strong interaction between the outgoing quarks, the following perturbative expansion for R has been obtained[45–47]:

$$R_{\mathrm{QCD}} = 3\sum_{i=1}^{n_f}\left(\frac{\beta_i(3-\beta_i^2)}{2}\right)Q_i^2\left[1 + f(\beta_i)\frac{\alpha_s(s)}{\pi} + C_2\left(\frac{\alpha_s(s)}{\pi}\right)^2\right] \quad . \qquad \text{[VI.2]}$$

where:

$$f(\beta) = \frac{2\pi^2}{3\beta} - (3+\beta)\left(\frac{\pi^2}{6} - \frac{1}{4}\right) \quad , \qquad \text{[VI.3]}$$

and $\alpha_s(s)$ is the energy-dependent strong coupling constant. Calculated in the modified minimal subtraction (MS) scheme,[48] the coefficient C_2 is given by:

$$C_2 = 1.986 - 0.115 n_f \quad . \qquad \text{[VI.4]}$$

According to the theory of QCD, α_s satisfies the renormalization group equation[49]:

$$2s\frac{\partial\alpha_s(s)}{\partial s} = b_0\alpha_s^2 + b_1\alpha_s^3 + b_2\alpha_s^4 \quad . \qquad \text{[VI.5]}$$

The coefficients b_0 and b_1 do not depend upon the renormalization scheme and are given by[50]:

$$b_0 = -\frac{1}{2\pi}\left[11 - \frac{2}{3}n_f\right] , \qquad \text{[VI.6]}$$

$$b_1 = -\frac{1}{4\pi^2}\left[51 - \frac{19}{3}n_f\right] . \qquad \text{[VI.7]}$$

The b_2 coefficient is computed in the framework of the $\overline{\text{MS}}$ renormalization scheme and is found to be[49]:

$$b_2 = -\frac{1}{64\pi^3}\left[2857 - 525n_f + \frac{269}{27}n_f^2\right] . \qquad \text{[VI.8]}$$

The expression for $\alpha_s(s)$ computed at an arbitrary center-of-mass energy $\sqrt{s}$ is given in terms of $\alpha_s(s_0)$ ($s_0 \equiv (6\ \text{GeV})^2$) as[49]:

$$\frac{1}{\alpha_s(s)} = \frac{1}{\alpha_s(s_0)} - \frac{b_0}{2}\ln\left[\frac{s}{s_0}\right] - \frac{b_1}{b_0}\ln\left[\frac{\alpha_s(s)}{\alpha_s(s_0)}\right] - \frac{1}{b_0^2}(b_2b_0 - b_1^2)(\alpha_s(s) - \alpha_s(s_0)) . \qquad \text{[VI.9]}$$

Using $\alpha_s(s_0)$ as an initial estimate, $\alpha_s(s)$ is solved for by iteration, using [VI.9]. R_{QCD} is then determined through Eq. [VI.2] at each of the center-of-mass energies listed in Table VI. Through the fitting procedures described below, $\alpha_s(s_0)$ is then estimated.

Two different fitting procedures are utilized to determine $\alpha_s(s_0)$. The first method used a χ^2-minimization technique. The χ^2 is constructed from two terms,

χ^2_{norm}, which depends only on the overall normalization of *R*, and contains the scale error δS = 5.2%, and χ^2_{shape}, which depends only upon the variation of *R* with energy and is independent of the overall normalization:

$$\chi^2 = \chi^2_{norm} + \chi^2_{shape} \quad , \qquad \text{[VI.10]}$$

where

$$XL\text{-}m = \frac{(\sum_i R_i - \sum_i T_i)^2}{(\delta S \sum_i R_i)^2 + \sum_i \delta R_i^2} \quad , \qquad \text{[VI.11]}$$

and

$$\chi^2_{shape} = \sum_i \frac{\left(R_i - \frac{\sum_j R_j}{\sum_j T_j} T_i\right)^2}{\delta R_i^2} \quad , \qquad \text{[VI.12]}$$

and where R_i and T_i denote the measured and predicted values of *R*, respectively, at each center-of-mass energy $\sqrt{s_i}$, and δR_i is the quadratic sum of the statistical and point systematic errors on *R*.

In the second method, a maximum likelihood fitting procedure is used to determine $\alpha_s(s_0)$. The likelihood is defined as follows:

$$L = \int_0^\infty dS \exp\left\{-\frac{1}{2}\left(\left(\frac{S-1}{\delta S}\right)^2 + \sum_i \left(\frac{S \cdot R_i - T_i}{S \delta R_i}\right)^2\right)\right\} \quad , \qquad \text{[VI.13]}$$

where the parent distribution of the scale variable S is assumed to be Gaussian, with a mean value of **1.0** and a standard deviation δS of 5.2%.

Table VIII shows the values of $\alpha_s(s_0)$ obtained from fitting the combined Run **1** and Run 2 data using the techniques described above. The χ^2_{tot} and maximum likelihood procedures yield virtually identical results. The mean value of $\alpha_s(s_0)$ obtained from the two different fitting procedures is

$$\alpha_s(s_0) = \mathbf{0.12 \pm 0.11} \quad , \qquad \text{[VI.14]}$$

where the error reflects the combined statistical, point and scale uncertainties of the measurement.

The stability of this result against changes to input parameter values is checked. First, the overall scale error is varied. For assumed scale errors of $\pm 3.0\%$ and $\pm 7.0\%$, the likelihood fit yields $\alpha_s(s_0) = 0.10 \pm 0.07$ and $\alpha_s(s_0) = 0.13 \pm 0.12$, respectively. As δS is increased further, the likelihood fit result approaches that of the χ^2_{shape} fit, as expected. Next, the charmed quark mass, assumed to be 1.4 GeV/c^2, is varied. The likelihood fit yields $\alpha_s(s_0) = 0.11 \pm 0.11$ and $\alpha_s(s_0) = 0.13 \pm 0.09$ corresponding to charmed quark masses of 1.2 and 1.6 GeV/c^2, respectively. Finally, varying the number of quark flavors from $n_f = 5$ (as prescribed[49] by the $\overline{\mathrm{MS}}$ renormalization scheme for this energy range) to $n_f = 4$, yields $\alpha_s(s_0) = 0.12 \pm 0.11$. Thus, the fitted value for $\alpha_s(s_0)$ is insensitive to moderate variations of input parameter values.

In Fig. 16, the predictions for *R* based on different values for $\alpha_s(s_0)$ are overlaid on the various experimental measurements. The dashed-dot curve represents the QPM ($\alpha_s = 0$) prediction for a charmed quark mass of 1.4 GeV. All the data shown in this figure are consistent with positive $\alpha_s(s_0)$. The solid curve in Fig. 16 is the QCD prediction for *R* resulting from the best fit value for $\alpha_s(s_0)$, 0.12. Nearly all the data in this figure are consistent with this prediction for *R*, with the exception of the Mark I[3] data, which are approximately 16% higher than the QCD prediction.

A 90% confidence level (C.L.) upper limit on $\alpha_s(s_0)$ is obtained by integrating the likelihood function (Eq. [VI.13]) from $\alpha_s(s_0) = 0$ to a value of $\alpha_s(s_0)$ corresponding to 90% of the total integral, giving $\alpha_s(s_0) < 0.24$. This result is

somewhat lower than the 68% C.L. limit of $\alpha_s < 0.33$ quoted in Ref. 41, for $7.4 < \sqrt{s} < 9.4$ GeV. The result obtained for R_{QCD} using the 90% C.L. limit on $\alpha_s(s_0)$ is shown as a dotted curve on Fig. 16. With the exception of the MARK I data, all the measurements in this energy range are compatible with this predict ion.

Equation [VI.9] may be used to extrapolate α_s from $\sqrt{s} = 6.0$ GeV to other energies. In so doing, α_s is required to be continuous across quark flavor thresholds. At $\sqrt{s} = 34.0$ GeV, the likelihood fit yields a, = $.09^{+.05}_{-.08}$. Expressed as an upper limit, the result is $\alpha_s < 0.14$ at 90% C.L. The CELLO group has recently fitted all available R-measurements from PETRA and PEP to determine α_s. The fit to the combined data yields[54] $\alpha_s(\sqrt{s} = 34 \text{ GeV}) = 0.17 \pm 0.03$. The Crystal Ball measurement of $\alpha_s(s_0)$ is compatible with the values obtained from the higher energy measurements, within the stated errors which are dominated by systematics.

VI.3 Summary and Acknowledgments

The Crystal Ball experiment has measured R over the range $5.0 < \sqrt{s} < 7.4$ GeV. No significant structure is visible above the QCD continuum. The average value of R in this energy range is $R = 3.44 \pm 0.03_{stat} \pm 0.01_{point-sys} \pm 0.18_{scale}$. The scale error in this measurement is considerably smaller than those of previous measurements in the same energy range. In a fit of R_{QCD} to the data, we obtain $\alpha_s = 0.12 \pm 0.11$ at $\sqrt{s} = 6.0$ GeV, where the error in α_s is dominated by the $\pm 5.2\%$ scale error in R. Within the range of the errors, this result agrees with measurements of a, at higher energies.

We gratefully acknowledge the efforts of A. Baumgarten and J. Broeder (SLAC) and B. Beron, E. B. Hughes, and R. Parks (High Energy Physics Laboratory, Stanford University), as well as those of the linac and SPEAR staff at the Stanford Linear Accelerator Center. We also thank R. Cowan for his invaluable aid during the typesetting of the manuscript.

This work is supported in part by the US Department of Energy under contracts DE–AC03–76SF00515 (SLAC), DE–AC02–76ER03064 (Harvard), DE AC03–81ER40050 (CIT), and DE–AC02–76ER03072 (Princeton); by the National Science Foundation under contracts PHY81–07396 (HEPL), PHY79–16461 (Princeton), and PHY75–22980 (CIT); and by the NATO fellowship (H.K.) and the Chaim Weizman Fellowship (F.P.).

We gratefully acknowledge the efforts of A. Baumgarten and J. Broeder (SLAC) and B. Beron, E. B. Hughes, and R. Parks (High Energy Physics Laboratory, Stanford University), as well as those of the linac and SPEAR staff at the Stanford Linear Accelerator Center. We also thank R. Cowan for his invaluable aid during the typesetting of the manuscript.

APPENDIX A. Radiative Correction Procedure:

This appendix outlines the method used to extract σ^0_{had} from the observed hadronic cross section, σ^{obs}_{had}. The leading-order initial state radiative correction factor δ may be written as a sum of terms

$$\delta = \delta_{vert} + \delta^e_{vac} + \delta^\mu_{vac} + \delta^\tau_{vac} + \delta^{had}_{vac} + \delta_\gamma \quad . \qquad [A.1]$$

Collectively referred to as δ_{virt}, the first five terms in this sum correspond to the virtual processes shown in Figs. 13(b–c). These diagrams contribute to the order-a radiative correction by interfering with the lowest-order process shown in Fig. 13(a). Since no real photon is emitted in these processes, the kinematics of the produced hadronic system is not altered and these corrections may be computed independently of the detect or's geometry.

The first term in [A.1], the initial state vertex correction, contains an infrared divergence which cancels a corresponding divergence in the bremsstrahlung term. The finite remainder is[55]

$$\delta_{vert}(s) = \frac{2\alpha}{\pi}\left[\frac{3}{4}\log\left(\frac{s}{m_e^2}\right) + \frac{\pi^2}{6} - 1\right] \quad . \qquad [A.2]$$

The next four terms arise from modifications to the virtual photon propagator due to e, μ, τ and hadron loops. These terms can be evaluated through a dispersion relation[56]

$$\delta^X_{vac} = \frac{-s}{2\pi^2\alpha}\int_{s_{th}}^{\infty} ds' \frac{\sigma_X(s')}{s' - s - i\epsilon} \quad , \qquad [A.3]$$

where σ_X is the lowest-order e^+e^- annihilation cross section into the final state X, and s_{th} is the threshold center-of-mass energy squared. For the production of a pair of leptons, each of mass m, $s_{th} = 4m^2$ and σ_X is given by

$$\sigma_X(x,s) = \frac{4\pi\alpha^2}{3s}\sqrt{1-x}(1+ \text{x,2}) \ , \qquad [A.4]$$

where $x = s_{th}/s$. In this case, the dispersion integral can be computed analytically, and the result is[37]

$$\delta^l_{vac}(x) = \frac{2\alpha}{\pi}\left\{-\frac{5}{9} - \frac{x}{3} + \frac{\sqrt{1-x}(2+x)}{6}\log\left[\frac{1+\sqrt{1-x}}{1-\sqrt{1-x}}\right]\right\} \quad \text{if x} \leq 1, \qquad [A.5]$$

$$= \frac{2\alpha}{\pi}\left\{-\frac{5}{9} - \frac{x}{3} + \frac{\sqrt{x-1}(2+x)}{3}\tan^{-1}\cdot\frac{1}{\sqrt{x-1}}\right\} \quad \text{if x > 1.} \qquad [A.6]$$

When $s \gg 4m^2$, Eq. $[A.5]$ reduces to

$$\delta^l_{vac}(s) = \frac{2\alpha}{\pi}\left\{-\frac{5}{9} + \frac{1}{3}\log\frac{s}{m^2}\right\} \ . \qquad [A.7]$$

Using Eq. $[A.6]$, the vacuum polarization contribution from heavy quarks with masses greater than 25.0 GeV is found to be negligible. Altogether, the sum of the vertex and lepton-loop corrections varies from 10.1% at $\sqrt{s}$ = 5.0 GeV to 10.9% at $\sqrt{s}$ = 7.4 GeV.

As shown in Eq. $[A.3]$, the hadronic vacuum polarization-loop correction requires knowledge of $\sigma^0_{had}(s')$ at other center-of-mass energies $\sqrt{s'}$. The computation of the hadronic vacuum polarization δ^I_{vac} used in the Monte Carlo simulation of initial state radiation is described in Ref. 39. δ^I_{vac} varies smoothly from +2.5% at $\sqrt{s}$ = 5.0 GeV to +3.0% at $\sqrt{s}$ = 7.4 GeV.

Using R measurements from this analysis, together with those from other energy regions,[54,57,58] a smoothed representation of R, denoted as $\widetilde{R}$, is obtained, and is shown in Fig. 14. Using $\widetilde{R}$, a second estimate of δ_{vac}^{had}, referred to as δ_{vac}^{II}, can be obtained by a piecewise evaluation of the dispersion integral in Eq. [A.3]. The components include

1. A continuum part below $\sqrt{s}$ = 36.0 GeV, which is evaluated numerically, ---using $\widetilde{R}$, as shown in Fig. 14;

2. A continuum part above $\sqrt{s}$ = 36.0 GeV, which is evaluated analytically, assuming R = 3.93.

3. A contribution from the narrow $q\bar{q}$ resonances w, ϕ, J/ψ, ψ', Υ, $\Upsilon(2s)$, $\Upsilon(3s)$, $\Upsilon(4s)$, $\Upsilon(5s)$ and $\Upsilon(6s)$ which is evaluated by substituting the Breit-Wigner cross section

$$\sigma_{tot,j}^{res}(s) = \frac{12\pi\Gamma_j^{ee}\Gamma_j^{tot}}{(s-M_j^2)^2 + (M_j\Gamma_j^{tot})^2} \qquad [A.8]$$

into Eq. [A.3], giving[37]

$$\delta_{vac}^{res}(s) = \sum_j \frac{6\Gamma_j^{ee}}{\alpha M_j} \frac{s[s - M_j^2 + \Gamma_j^{tot} M_j \pi^{-1} \log(s/M_j^2)]}{(s-M_j^2)^2 + (M_j\Gamma_j^{tot})^2} \quad , \qquad [A.9]$$

where Γ_j^{ee} and Γ_j^{tot} is the electronic- and total width, respectively, of the j^{th} resonance, and M_j is the pole mass.

At $\sqrt{s}$ = 6.0 GeV, the hadronic vacuum polarization contribution from the continuum is +2.0%; the narrow resonance contribution is +0.4%. δ_{vac}^{II} varies from +2.3% at $\sqrt{s}$ = 5 GeV to +2.5% at $\sqrt{s}$ = 7.4 GeV.

The bremsstrahlung correction factor results from the radiation of a real photon by the initial state charged particles. After integrating over the angular distribution of the radiated photon, the bremsstrahlung correction δ_γ is given by[55]

$$\delta_\gamma(s) = \int_0^{k_{max}} G(s,k)\,dk \quad , \qquad [A.10]$$

$$G(s,k)\,dk = t\left[1 - k + \frac{k^2}{2}\right]\frac{\sigma^0_{had}(s')}{\sigma^0_{had}(s)}\frac{dk}{k} \quad , \qquad [A.11]$$

$$t = \frac{2\alpha}{\pi}\left[\log\left(\frac{s}{m_e^2}\right)\right] \quad , \qquad [A.12]$$

$$s' = s(1-k) \quad , \qquad [A.13]$$

where s' is the center-of-mass energy squared of the e^+e^- collision after radiation, and the quantity t, the equivalent radiator, varies from 0.081 at $\sqrt{s}$ = 5.0 GeV to 0.084 at $\sqrt{s}$ = 7.4 GeV.

For small k, $G(s, k) \approx t/k$, and therefore δ_γ is infrared-divergent. This divergence is cancelled by the divergent part of the vertex correction. The term δ_γ in Eq. [A.1] refers to the finite part of the bremsstrahlung correction. Assuming $\sigma^0_{had}(s') \sim 1/s'$, the bremsstrahlung integral can be evaluated analytically. The result is

$$\delta_\gamma^{1/s}(k_{max}) = t \cdot \left[\log k_{max} - \frac{k_{max}}{2} - \frac{1}{2}\log(1 - k_{max})\right] \quad . \qquad [A.14]$$

The Monte Carlo simulation of initial state radiation from Ref. 59 is used to estimate the function $c(k)$. In this simulation, the photon energy fractions

are generated up to a value of k_{max} given by $k_{max} = 1 - s_{min}/s$, where $s_{min} = 1.0\ \mathrm{GeV}^2$. The maximum photon energy fraction varies from 0.96 at 5.0 GeV to 0.98 at 7.4 GeV. The relative efficiency $\epsilon(k)/\epsilon(0)$ is, to a very good approximation, independent of the model used to generate the photon energies. The relative efficiency factor as determined at $\sqrt{s}$ = 7.4 GeV is shown in Fig. 15, and is characteristic of the distributions obtained at other energies. For photon energy fractions near k_{max}, the relative efficiency is very small (cf. Fig. 15), thus rendering the product $\bar{\epsilon}_{had} \cdot (1 + \delta)$ insensitive to the exact choice of k_{max}.

In the Monte Carlo simulation of initial state radiation, an exponentiated form[59] for δ_γ is used. In the spectral distribution $G(s, k)$, $\sigma^0_{had}(s')$ is assumed to vary as $1/s'$. The result obtained for δ_γ from the Monte Carlo is virtually identical to the one calculated using the unexponentiated form, Eq. [A.14].

The emission of a bremsstrahlung photon from one of the incoming charged leptons lowers the collision energy of the e^+e^- pair and therefore produces a correction which depends on the leading-order cross section $\sigma^0_{had}(s')$ at lower center-of-mass energies. Since the kinematics of the hadronic system is altered, it is useful to redefine the bremsstrahlung correction to explicitly include efficiency effects. This is accomplished by rewriting Eq. [V.8] as

$$\sigma^{obs}_{had} = \sigma^0_{had} \cdot \epsilon(0) \cdot (1 + \delta_{virt} + \delta_{\gamma obs}) \quad , \qquad [A.15]$$

where $\delta_{\gamma obs}$ is a convolution of the hadronic detection efficiency $\epsilon(k)$ expressed as a function of *k*, the fraction of the incident beam energy carried off by the radiative photon, and the spectral distribution of the bremsstrahlung radiation. The quantity e(O), the efficiency to detect a nonradiative event, is estimated

by *LUND* 4.3 to be (94.2 $\pm$ 0.3)%. Within the precision of the Monte Carlo estimate, $\epsilon(0)$ is independent of $\sqrt{s}$.

To obtain the observed bremsstrahlung correction $\delta_{\gamma obs}$, the relative efficiency $\epsilon(k)/\epsilon(0)$ is inserted into Eqs. [A.10] and [A.11] to give

$$\delta_{\gamma obs}(s) = t \int_0^{k_{max}} \frac{dk}{k} \left[1 - k + \frac{k^2}{2}\right] \frac{\sigma^0_{had}(s')}{\sigma^0_{had}(s)} \frac{\epsilon(k)}{\epsilon(0)} \quad . \qquad [A.16]$$

The cross section $\sigma^0_{had}(s')$ is written as a sum of $\widetilde{R}$. $\sigma^0_{\mu\mu}$ and narrow vector resonance cross sections $\sigma^{res}_{had,j}$. The integration over $\widetilde{R}\cdot\sigma^0_{\mu\mu}$ is performed numerically, while the contributions from radiation down to the narrow vector resonances are computed analytically. Substituting

$$\sigma^{res}_{had,j}(s') = \frac{12\pi\Gamma^{ee}_j\Gamma^{had}_j}{(s' - M_j^2)^2 + (M_j\Gamma^{tot}_j)^2} \qquad [A.17]$$

into [A.16] and integrating, the contribution to $\delta_{\gamma obs}$ from the radiative tails of the narrow resonances is

$$\delta^{res}_{\gamma obs}(s) = t\frac{12\pi^2}{\epsilon(0)R(s)} \sum_j \frac{\Gamma^{ee}_j\Gamma^{had}_j}{\Gamma^{tot}_j M_j}\left[1 - k_j + \frac{k_j^2}{2}\right]\frac{\epsilon(k_j)}{k_j} \quad , \qquad [A.18]$$

$$k_j = 1 - \frac{M_j^2}{s} \quad .$$

The narrow resonance contribution varies from +1.4% at 5.0 GeV to +0.4% at 7.4 GeV, while $\delta_{\gamma obs}$ varies from -1.0% to +0.2% over the same energy region. This result is combined with the vacuum polarization estimate δ^{II}_{vac} to compute $\bar{\epsilon}_{had}$. (1 + S). The computed values of $\bar{\epsilon}_{had}$. (1 + δ) are shown as solid points in Fig. 10(c). A second-order polynomial fit to these points, represented by the

solid curve, is used to interpolate to intermediate &-values. By comparison, the dashed curve is obtained from a $1/s'$ parameterization of $\sigma^0_{had}(s')$ in Eq. [A.16], together with the hadronic vacuum polarization computation from Ref. 39.

In summary, the radiative correction factor $\bar{\epsilon}_{had} \cdot (1 + \delta)$ is computed using two different models for the underlying cross section $\sigma^0_{had}(s)$. While the terms $\bar{\epsilon}_{had}$ and $(1 + \delta)$ depend on the modeling of $\sigma^0_{had}(s)$, the product is nearly model-independent, and ranges in value from 1.04 to 1.07 in this measurement.

REFERENCES

1) S. D. Drell, D. J. Levy, and T. M. Yan, *Phys. Rev.* **187,** 2159 (1969).

2) We take for the up-, down-, strange- and charmed-quark masses the values 0.3, 0.3, 0.5 and 1.4 GeV, respectively.

3) J. L. Siegrist et al., *Phys. Rev.* **D26, 969** (1982).

4) R. M. Barnett, M. Dyne, and L. McLerran, *Phys. Rev.* **D22, 594** (1980).

5) M. Oreglia *et al., Phys. Rev.* **D25, 2259** (1982).

6) J. E. Gaiser *et al., Phys. Rev.* **D34,** 711 (1986).

7) A. J. Weinstein, *A Study of Two-Photon Scattering into All-Neutral Final States Using the Crystal* Ball, Ph.D. thesis, Harvard University (1983).

8) A. J. Weinstein *et al., Phys. Rev.* **D28, 2896** (1983).

9) J. F. Crawford *et al., Nucl. Inst. and Meth.* **127, 173** (1975).

10) F. A. Berends, K. J. F. Gaemers, and R. Gastmans, *Nucl. Phys.* **B68, 541 (1976).**

11) F. A. Berends and R. Kleiss, *Nucl. Phys.* **B228, 537 (1983).**

12) A connected region is defined to be a group of adjacent crystals each having at least 10 MeV of deposited energy.

13) J. Gaiser, *Charmonium Spectroscopy from Radiative Decays of the J/ψ and ψ',* SLAC Report SLAC-255 (August 1982).

14) F. A. Berends and R. Kleiss, *Nucl. Phys.* **B228, 537 (1983).**

15) F. A. Berends and R. Kleiss, *Nucl. Phys.* **B186, 22 (1981).**

16) The typical horizontal and vertical sizes of the beams at the interaction region are 500 μm and 50 μm, respectively.

17) R. L. Ford and W. R. Nelson, *The EGS Code System: Computer Programs for the Monte Carlo Simulation of Electromagnetic Cascade Showers (Version 3)*, SLAC-0210 (June 1978).

18) H. Kolanoski, private communication.

19) R. Kleiss, private communication.

20) Cosmic ray data were collected during periods when there were no stored beams at SPEAR.

21) T. Sjöestrand and M. Bengtsson, Comp. *Phys. Comm. 27, 243* (1982).

22) T. Sjöestrand, Comp. *Phys. Comm. 28, 229* (1983).

23) F. A. Berends and R. Kleiss, *Nucl. Phys.* B177, 237 (1981).

24) F. A. Berends, R. Kleiss, S. Jadach and Z. Was, *Acta Phys. Polon.* B14, 413 (1983).

25) Y. S. Tsai, *Phys. Rev.* D4, 2821 (1971).

26) C. A. Blocker *et al., Phys. Rev. Lett. 49,* 1369 (1983).

27) We wish to thank D. Burke and L. Golding for making their Monte Carlo program available to us.

28) S. J. Brodsky *et al., Phys. Rev.* D4, 1532 (1971).

29) C. Berger *et al., Phys. Lett.* **89B**, 120 (1979).

30) C. Berger *et al., Phys. Lett.* **99B**, 287 (1980).

31) B. Anderson, G. Gustafson, and T. Sjöestrand, *Nucl. Phys.* **B197, 45** (1982).

32) C. Peterson, D. Schlatter, I. Schmitt, and P. M. Zerwas, *Phys. Rev.* **D27**, 105 (1983).

33) G. S. Abrams *et al., Phys. Rev. Lett. 44,* 10 (1980).

34) In this experiment, the sphericity is approximated as $S = 1.5 \cdot P_{t\text{-}jet}^2 / \sum_k E_k^2$.

35) T. A. Gabriel, Oak Ridge National Laboratory Report ORNL/TM-9727 (1985); CCC-178 (1977).

36) T. D. Lee and M. Nauenberg, *Phys. Rev.* 133, 1549 (1964); T. Kinoshita, *J. Math. Phys. 3, 650* (1962).

37) Y. S. Tsai, SLAC-PUB-3129 (1983).

38) E. A. Kuraev and V. S. Fadin, Sov. *J. N&l. Phys.* **41, 466** (1985).

39) F. A. Berends and G. J. Komen, *Phys. Lett.* **63B, 432** (1976).

40) C. Berger *et al., Phys. Lett.* **B81, 410** (1979).

41) B. Niczyporuk *et al., Z. Phys.* **C15, 299** (1982).

42) H. Albrecht *et al., Phys. Lett.* **B116, 383** (1982).

43) P. Bock *et al., Z. Phys.* C6, 125 (1980).

44) Z. Jakubowski *et al., Z. Phys.* **C40**, *49* (1988).

45) M. Dine and J. Saperstein, *Phys. Rev. Lett. 43, 668* (1979);
K. G. Chetyrkin *et al., Phys. Lett.* **85B, 277** (1979);
W. Celmaster and R. J. Gonsalves, *Phys. Rev. Lett.* **78B, 132** (1978).

46) J. Schwinger, *Particles, Sources and Fields* (Addison-Wesley, New York, 1973), Vol. II, Chaps. 4 and 5.

47) T. Appelquist and H. D. Politzer, *Phys. Rev. Lett.* 34, 43 (1975).

48) W. A. Bardeen *et al., Phys. Rev.* **D18, 3998** (1978).

49) W. Marciano, *Phys. Rev.* **D29, 580** (1984).

50) D. Gross and F. Wilczek, *Phys. Rev. Lett. 30,* 1343 (1973); *Phys. Rev.* **D8**, 3633 (1973);

H. D. Politzer, *Phys. Rev. Lett.* 30, 1346 (1973);

W. Caswell, *Phys. Rev. Lett. 33, 244* (1974);

D. R. T. Jones, *Nucl. Phys.* **B75, 531** (1974).

51) R. Brandelik *et al., Phys. Lett.* **113B, 499** (1982).

52) J. Burger *et al., Phys. Rev.* D34, 681 (1986).

53) R. Hollebeek *et* al., SLAC-PUB-2989 (1982).

54) H.-J. Behrend *et al., Phys. Lett.* **B183, 400** (1987).

55) G. Bonneau and F. Martin, *Nucl. Phys.* **B27, 381** (1971).

56) N. Cabibbo and R. Gatto, *Phys. Rev.* 124, 1577 (1961).

57) C. Bacci *et al., Phys. Lett.* **86B, 234** (1979),

58) A. Osterheld *et* al., SLAC-PUB-4160 (1986).

59) F. A. Berends and R. Kleiss, *Nucl. Phys.* **B178,** 141 (1981).

TABLE CAPTIONS

1. Large- and small-angle luminosities.

2. Beam-gas background. The error in f is half the difference between f_{data} and either $f_{\int Idt}$ or f_{PCT}. The error in $(N_{coll}-N_{bg})/\mathcal{L}$ reflects the statistical uncertainties in N_{coll}, N_{sep} and $\mathcal{L}$.

3. Backgrounds from τ decays and $\gamma\gamma$ collisions. The errors on the observed cross sections are due to Monte Carlo statistics.

4. R-values for different beam-gas cuts. Errors reflect the statistical uncertainties in N_{coll}, N_{sep} and $\mathcal{L}$.

5. Contributions to the systematic scale error in R.

6. R-values with statistical and point systematic errors.

7. $\alpha_s(\sqrt{s_0}$ = 6GeV) fit results.

Table I

$\sqrt{s}$ (GeV)	$\mathcal{L}_{\text{large}}$ (nb^{-1})	$\mathcal{L}_{\text{small}}$ (nb^{-1})	$\mathcal{L}$ (nb^{-1})
	Run 1		
5.20	78.0 ± 1.6	75.8	76.9 ± 0.8 ± 1.1
6.00	94.0 ± 2.0	95.9	95.0 ± 1.0 ± 1.0
6.50	91.6 ± 2.0	96.3	94.0 ± 1.0 ± 2.4
7.00	117.3 ± 2.5	121.9	119.6 ± 1.3 ± 2.3
Totals:	381 ± 4	390	386 ± 2
	Run 2		
5.00	168.1 ± 2.8	171.6	169.9 ± 1.4 ± 1.8
5.25	179.5 ± 3.0	181.3	180.4 ± 1.5 ± 0.9
5.50	196.8 ± 3.3	199.1	198.0 ± 1.6 ± 1.2
5.75	228.9 ± 3.8	229.8	229.4 ± 1.9 ± 0.5
6.00	234.8 ± 4.0	239.6	237.2 ± 2.0 ± 2.4
6.25	273.2 ± 4.5	274.0	273.6 ± 2.3 ± 0.4
6.50	299.8 ± 5.0	298.7	299.3 ± 2.5 ± 0.6
6.75	392.2 ± 6.3	401.4	396.8 ± 3.1 ± 4.6
7.00	339.8 ± 5.7	340.5	340.2 ± 2.9 ± 0.4
7.25	264.9 ± 4.7	272.8	268.9 ± 2.3 ± 4.0
7.40	1191.2 ± 17.2	1248.7	1220.0 ± 8.6 ± 28.8
Totals:	3769 ± 22	3858	3813 ± 11 ± 30

Table II

$\sqrt{s}$ (GeV)	N_{coll}	f	N_{sep}	N_{bg}	N_{bg}/N_{coll} (%)	$(N_{coll} - N_{bg})/\mathcal{L}$ (nb)
		Run1				
5.20	1094	2.04 ± 0.01	31	63	5.8	13.41 ± 0.48
6.00	1038	1.96 ± 0.08	34	67	6.4	10.23 ± 0.38
6.50	984	1.33 ± 0.07	93	124	12.6	9.16 ± 0.37
7.00	1135	1.43 ± 0.03	121	173	15.2	8.04 ± 0.32
		Run2				
5.00	2774	5.86 ± 1.19	58	340	12.3	14.33 ± 0.42
5.25	2722	3.06 ± 0.12	88	269	9.9	13.60 ± 0.35
5.50	2637	2.97 ± 0.36	90	267	10.1	11.97 ± 0.31
5.75	2831	6.37 ± 0.03	45	287	10.1	11.09 ± 0.31
6.00	2743	1.95 ± 0.28	143	279	10.7	10.39 ± 0.26
6.25	2852	2.03 ± 0.08	173	351	12.3	9.14 ± 0.23
6.50	2953	1.99 ± 0.05	190	378	12.8	8.60 ± 0.22
6.75	3565	1.56 ± 0.12	231	360	10.1	8.08 ± 0.17
7.00	2815	3.19 ± 0.20	98	313	8.2	7.36 ± 0.19
7.25	2102	2.42 ± 0.09	66	160	7.6	7.22' ± 0.20
7.40	9708	37.1 ± 1.00	46	1707	17.6	6.56 ± 0.23

Table III

$\sqrt{s}$ (GeV)	$N_{\tau\tau}/N_{coll}$ (%)	$N_{\gamma\gamma}/N_{coll}$ (%)	$(\epsilon\sigma)_{\tau\tau}+(\epsilon\sigma)_{\gamma\gamma}$ (nb)
	Run 1 Data		
5.20	10.1	2.6	1.81 ± 0.03
6.00	9.5	3.2	1.39 ± 0.02
6.50	8.2	3.2	1.20 ± 0.02
7.00	7.6	3.4	1.05 ± 0.02
	Run 2 Data		
5.00	9.6	2.3	1.94 ± 0.04
5.25	9.3	2.5	1.78 ± 0.03
5.50	9.5	2.7	1.63 ± 0.02
5.75	9.3	2.9	1.51 ± 0.02
6.00	9.5	3.2	1.39 ± 0.02
6.25	9.1	3.3	1.29 ± 0.02
6.50	8.8	3.4	1.20 ± 0.02
6.75	8.9	3.7	1.12 ± 0.02
7.00	8.9	3.9	1.05 ± 0.02
7.25	8.7	4.1	0.99 ± 0.02
7.40	8.2	4.0	0.95 ± 0.02

Table IV

$\sqrt{s}$ (GeV)	R_{soft}	R_{hard}	$R_{standard}$
	Run 2 Data		
5.0	3.62 ± 0.18	3.38 ± 0.09	3.42 ± 0.12
5.5	3.41 ± 0.16	3.26 ± 0.09	3.41 ± 0.10
6.0	3.81 ± 0.14	3.46 ± 0.09	3.50 ± 0.10
6.5	3.46 ± 0.14	3.27 ± 0.09	3.37 ± 0.10
7.0	3.29 ± 0.15	3.26 ± 0.10	3.35 ± 0.10
7.4	3.38 ± 0.26	3.29 ± 0.10	3.35 ± 0.14
Average:	3.52 ± 0.07	3.32 ± 0.04	3.40 ± 0.04

Table V

Source	% Error
Hadron efficiency estimate:	± 3.3
Luminosity:	f 2 . 7
Beam-gas subtraction:	f 2 . 2
Radiative corrections:	± 1.3
Tau-subtraction:	± 1.2
Two-photon subtraction:	± 1.0
Systematic error quadrature sum:	± 5.2

Table VI

$\sqrt{s}$ (GeV)	R	δR_{stat}	$\delta R_{point\,sys}$
	Run 1 data		
5.20	3.44	0.14	0.06
6.00	3.44	0.15	0.05
6.50	3.62	0.17	0.11
7.00	3.71	0.17	0.09
Average:	3.54	0.08	0.03
	Run 2 data		
5.00	3.42	0.12	0.12
5.25	3.57	0.11	0.03
5.50	3.41	0.10	0.06
5.75	3.44	0.11	0.02
6.00	3.50	0.10	0.08
6.25	3.31	0.10	0.03
6.50	3.37	0.10	0.03
6.75	3.42	0.09	0.06
7.00	3.35	0.10	0.04
7.25	3.57	0.11	0.07
7.40	3.35	0.14	0.10
Average:	3.43	-0.03	0.01
Combined average:	3.44	0.03	0.01

Table VII

Minimize:	$\alpha_s(s_0)$	Comment:
χ^2_{norm}	$0.10^{+.11}_{-.10}$	Depends only on the overall magnitude of R.
χ^2_{shape}	$0.18^{+.14}_{-.18}$	Depends only on the G-dependence of R.
χ^2_{tot}	$0.12^{+.10}_{-.11}$	Incorporates both the overall magnitude and &-dependence of R.
-2 log L	$0.11^{+.10}_{-.11}$	

FIGURE CAPTIONS

1. Schematic of the detector. Two of the four luminosity monitor counters are shown.

2. Development of the Ball geometry and nomenclature.

3. (a) Deposited shower energy fraction x_{13} and (b) $\cos\theta_z$ for QED Monte Carlo events (histogram) and data (solid circles) at $\sqrt{s}$ = 7.4 GeV.

4. Ratio of the large- to small-angle luminosity versus $\sqrt{s}$ for Run 1 (open circles) and Run 2 (solid circles). The errors represent only the statistical uncertainty on the ratio.

5. The energy asymmetry, *A*, plotted versus $P^2_{t\text{-}jet}$ for (a) cosmic-ray data and (b) *LUND* 4.3 Monte Carlo hadronic events generated at $\sqrt{s}$ = 5.0 GeV. The solid curve is defined by the equality in Eq. [IV.4].

6. The timing distribution for events where only energetic QED events have been removed (upper histogram); for events passing the cosmic-ray selection criteria (middle histogram); and for events passing all hadronic event selection criteria (lower histogram), at $\sqrt{s}$ = 7.4 GeV.

7. The distribution of the beam-gas q-function for separated-beam events (shaded histogram) and for *LUND* 4.3 Monte-Carlo generated hadronic events (unshaded histogram); both distributions correspond to a beam energy of 3.5 GeV.

8. Visible energy in the Ball, normalized to $\sqrt{s}$ at 7.0 GeV, (a) before and (b) after hadronic event selection. The shaded histogram in (b) shows the remnant beam-gas contamination. The solid curve in (b) is the hadronic

event detection efficiency determined from *LUND* 4.3, as described in Section V.3.

9. Produced and observed cross sections for $\tau\tau\gamma$ events (diamonds) and hadronic events from $\gamma\gamma$ collisions (squares). The sums of the observed cross sections are shown as open circles. The solid curves are fits to each set of cross sections and are used for interpolation.

10. (a) $\bar{\epsilon}_{had}$ calculated with resonances included in $\sigma^0_{had}(s')$. The Monte Carlo estimates are depicted as solid points; the solid curve is a fit to these points. (b) $(1+\delta)$ with resonances included in $\sigma^0_{had}(s')$ for the order-a case (solid curve); to all orders in the leading-log approximation (dotted curve). (c) $\bar{\epsilon}_{had} \cdot (1+\delta)$ using the order-a radiative correction with resonances included in $\sigma^0_{had}(s')$; the Monte Carlo estimates are depicted as solid points. The solid curve is a fit to these points and is used for interpolation. $\bar{\epsilon}_{had} \cdot (1+\delta)$ assuming a $1/s'$ dependence for $\sigma^0_{had}(s')$ (dashed curve).

11. Background subtracted distributions of x_{vis}, sphericity and the multiplicity of bump modules containing at least 50 MeV, for the data (solid points) at $\sqrt{s}$ = 5.5 GeV (a–c) and $\sqrt{s}$ = 7.0 GeV (d-f). The predictions of *LUND* 4.3 are also shown for $P = V$ (solid curves), $V = 0$ (dashed curves) and $P = 0$ (dashed-dotted curves).

12. (a) $P^2_{t\text{-}jet}$, (b) P^2_{t-z} and (c) energy asymmetry distributions from the background-subtracted data (solid circles) at $\sqrt{s}$ = 7.0 GeV. Predictions from *LUND* 4.3 with standard parameters are shown as solid curves. The dashed and dashed-dotted curves correspond to pure P and pure V parameterizations of *LUND* 4.3, respectively.

13. Diagrams included in the initial state radiative correction procedure for e^+e^- annihilation into hadrons: (a) lowest-order process; (b) vertex correction diagram; (c) vacuum polarization diagrams; and (d) bremsstrahlung diagram.

14. Smoothed R values used in the calculation of δ_{vac}^{II} and $\delta_{\gamma obs}$.

15. The relative hadron detection efficiency $\epsilon(k)/\epsilon(0)$ versus the radiative photon energy fraction k at $\sqrt{s}$ = 7.4 GeV.

16. Comparison of Crystal Ball Run 1 and Run 2 R-values with results from other experiments. All R-values have been r-subtracted and radiatively corrected. The vertical error bars represent only the statistical uncertainties on each data point. The open squares are averages of the MARK I data presented in Ref. 3, where the horizontal error bars indicate the $\sqrt{s}$-range over which the averages are performed. The solid curve represents the best fit of R_{QCD} to the combined Run 1 and Run 2 data with $\alpha_s(s_0)$ = 0.12. The dotted curve corresponds to $\alpha_s(s_0)$ = 0.24 (90% confidence level upper limit). The dashed-dotcurve is the R_{QPM} prediction (α_s = 0).

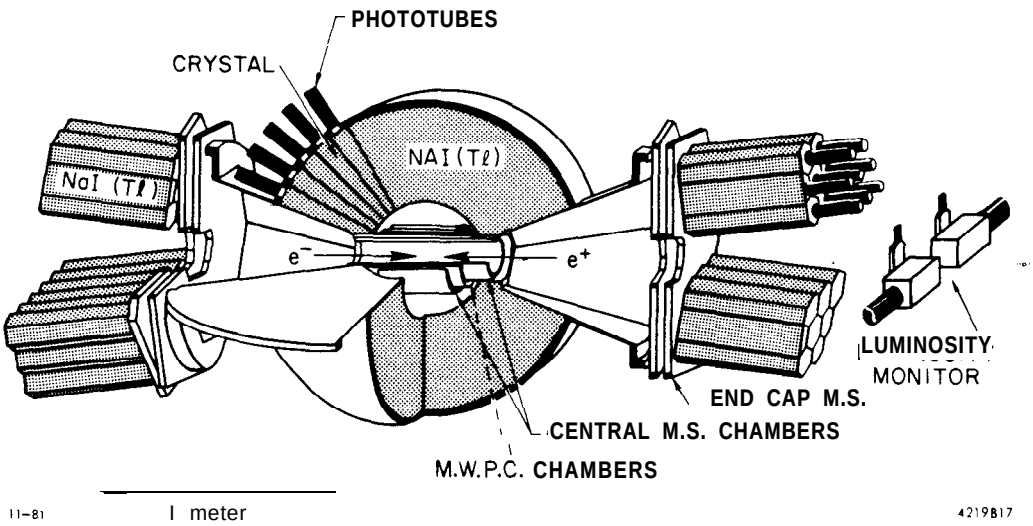
PHOTOTUBES
CRYSTAL
NaI (Tℓ)
NAI(Tℓ)
e⁻
e⁺
LUMINOSITY
MONITOR
END CAP M.S.
CENTRAL M.S. CHAMBERS
M.W.P.C. CHAMBERS
1 meter
11-81
4219B17

Fig. 1

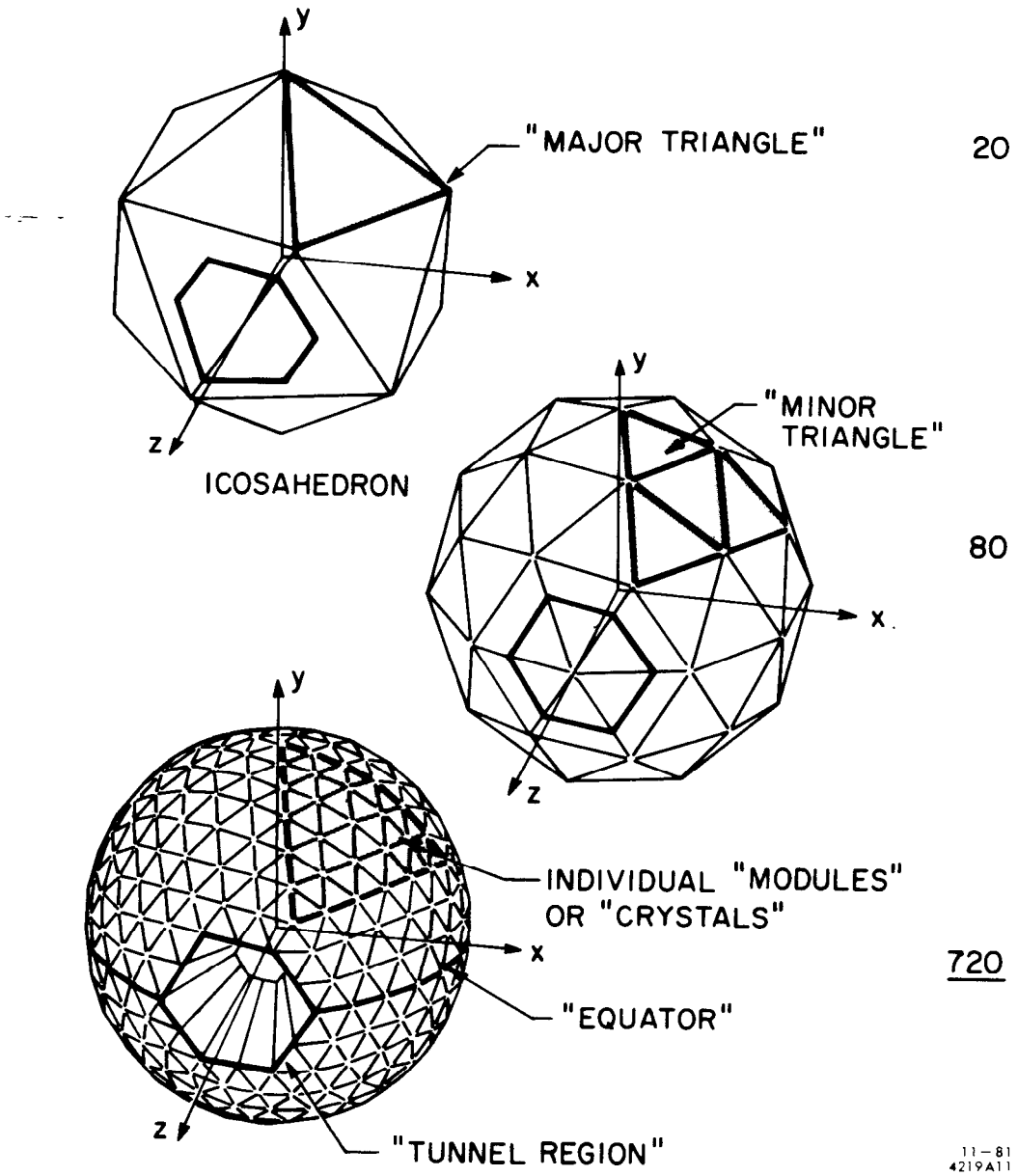
y
"MAJOR TRIANGLE"
20
x
z
ICOSAHEDRON
y
"MINOR
TRIANGLE"
80
x
z
y
INDIVIDUAL "MODULES"
OR "CRYSTALS"
x
720
"EQUATOR"
z
"TUNNEL REGION"
11-81
4219A11

Fig. 2

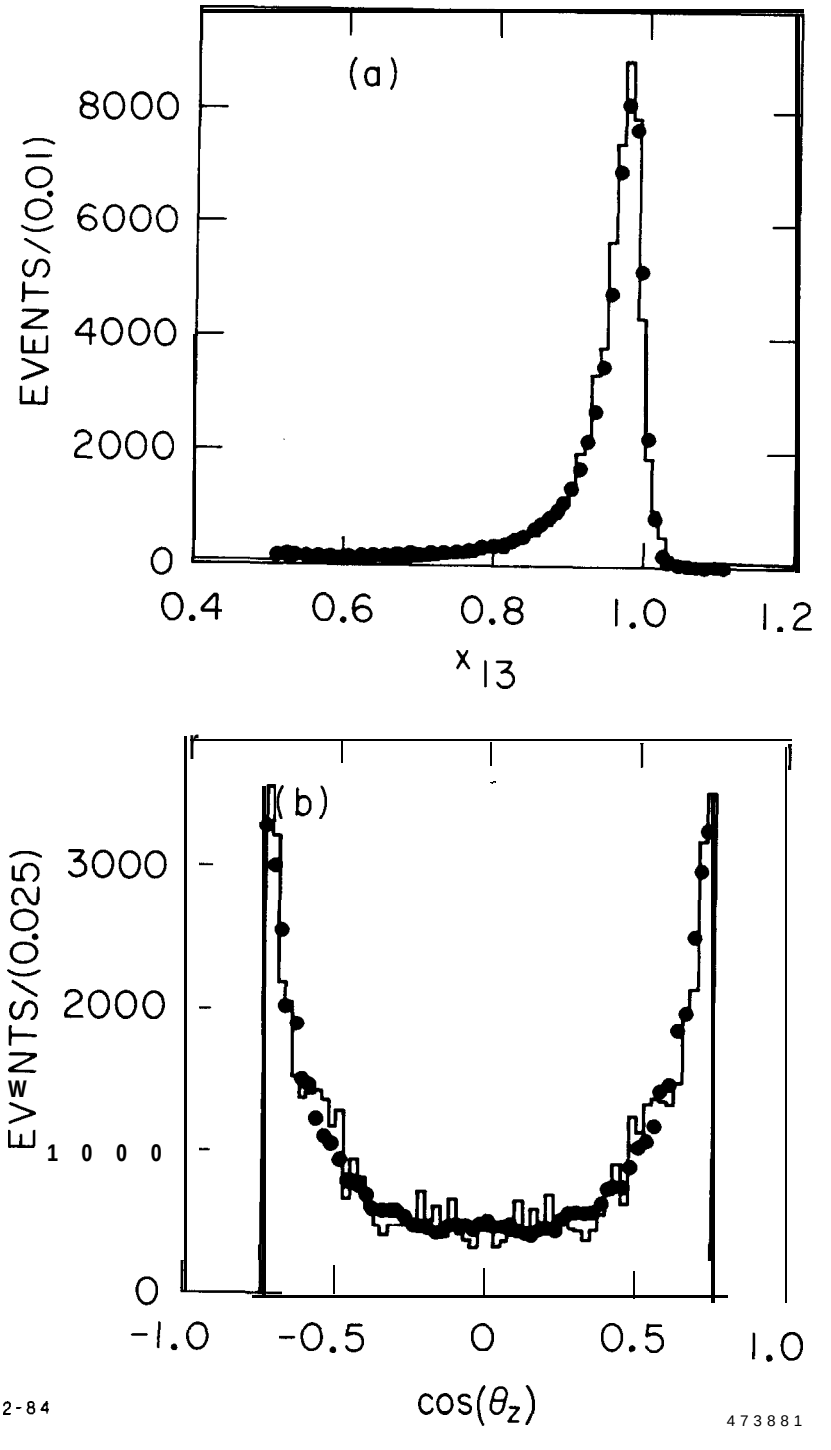
(a)
8000
6000
4000
2000
0
EVENTS/(0.01)
0.4
0.6
0.8
1.0
1.2
x13
(b)
3000
2000
1000
0
EVENTS/(0.025)
-1.0
-0.5
0
0.5
1.0
cos(θz)
2-84
473881

Fig. 3

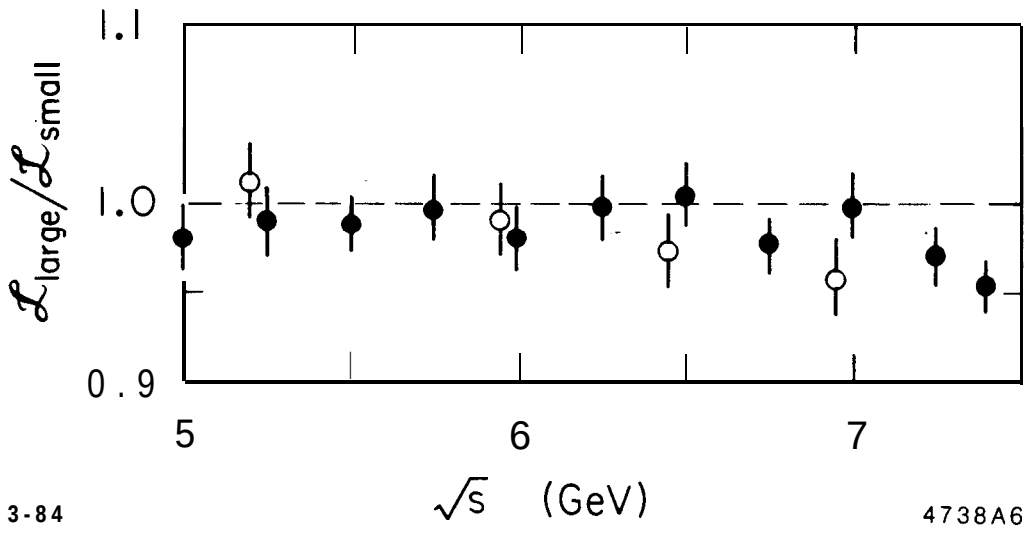
1.1
1.0
0.9
$\mathcal{L}_{large}/\mathcal{L}_{small}$
5
6
7
$\sqrt{s}$ (GeV)
3-84
4738A6

Fig. 4

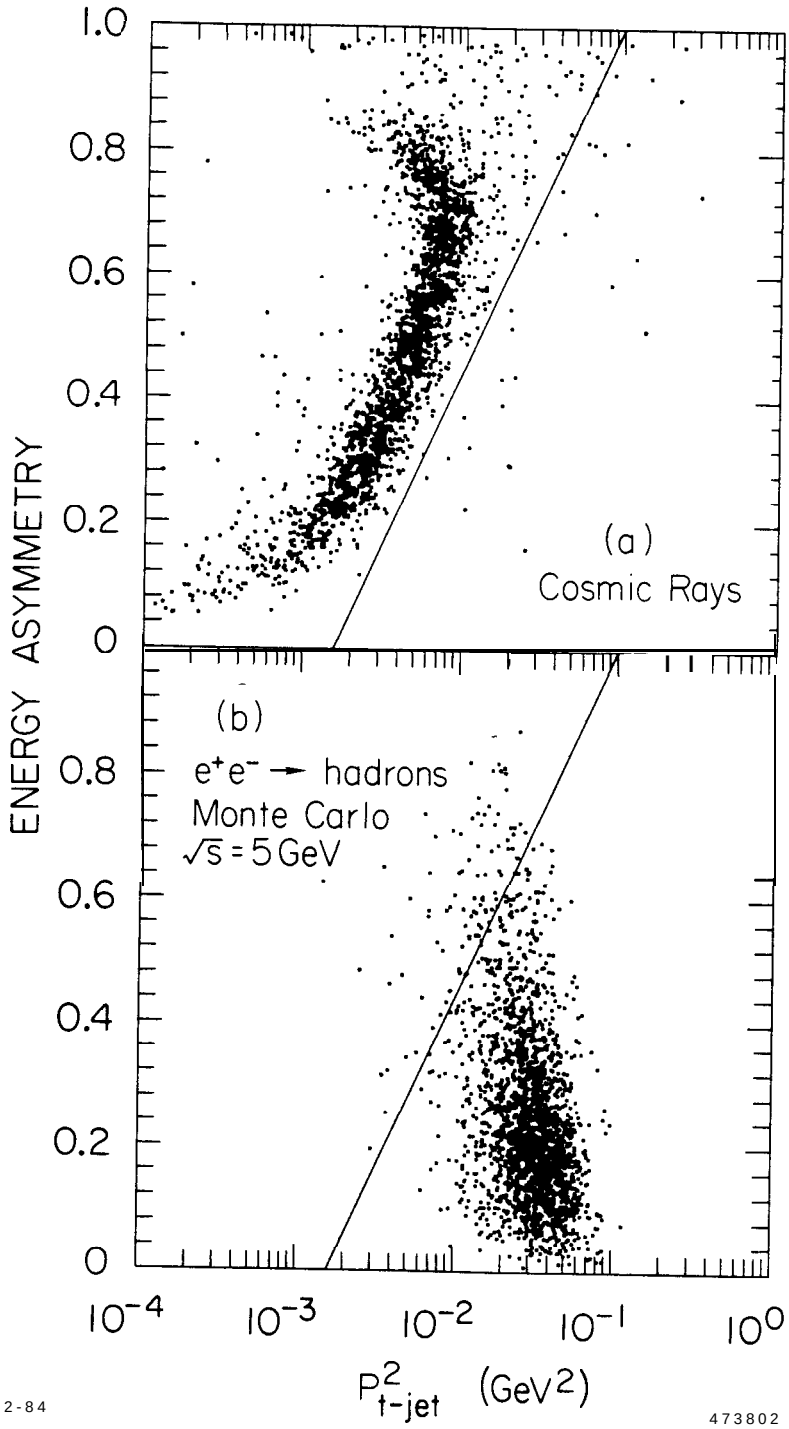
1.0
0.8
0.6
0.4
0.2
0
ENERGY ASYMMETRY
(a)
Cosmic Rays
(b)
e+e− → hadrons
Monte Carlo
√s = 5 GeV
0.8
0.6
0.4
0.2
0
10−4
10−3
10−2
10−1
100
P2t-jet (GeV2)
2-84
473802

Fig. 5

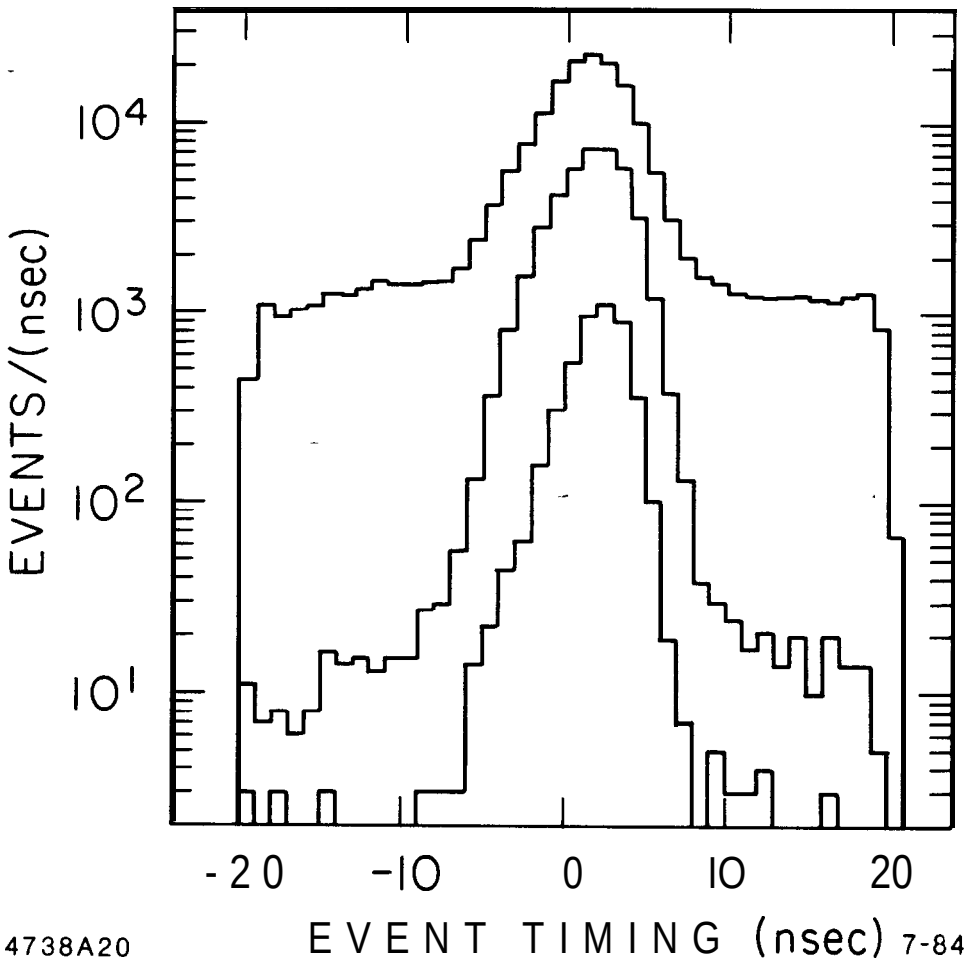
EVENTS/(nsec)
10^4
10^3
10^2
10^1
-20
-10
0
10
20
EVENT TIMING (nsec)
4738A20
7-84

Fig. 6

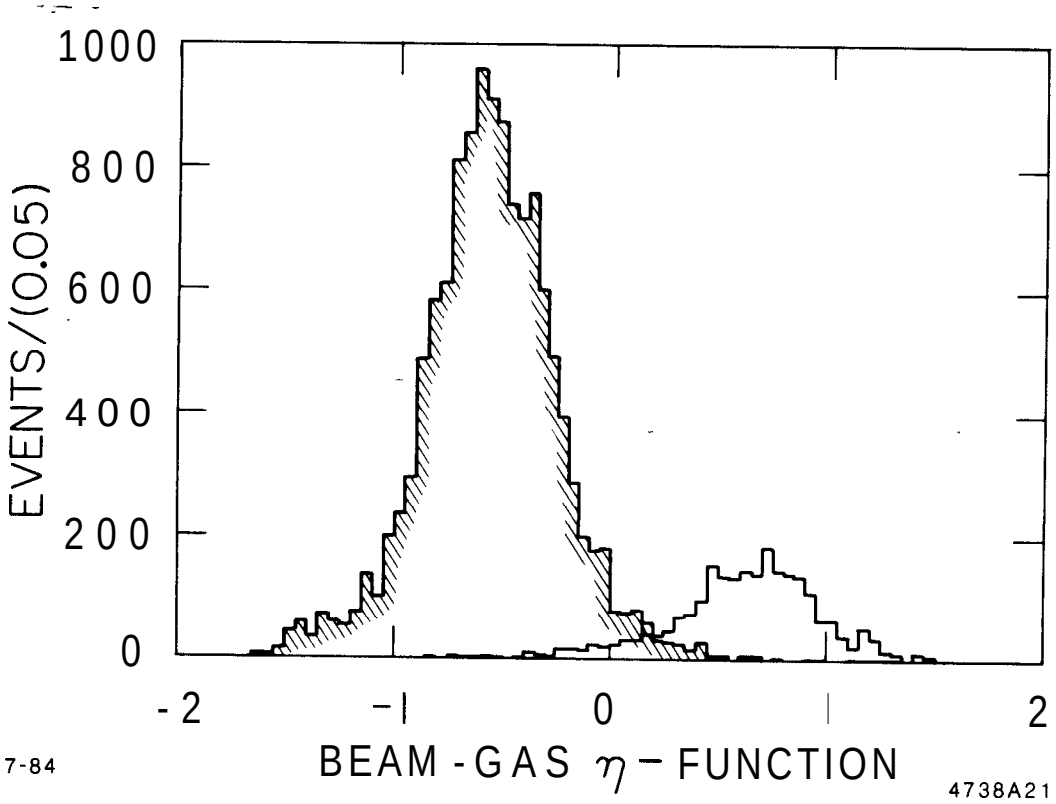
1000
800
600
400
200
0
EVENTS/(0.05)
-2
-1
0
2
BEAM-GAS η - FUNCTION
7-84
4738A21

Fig. 7

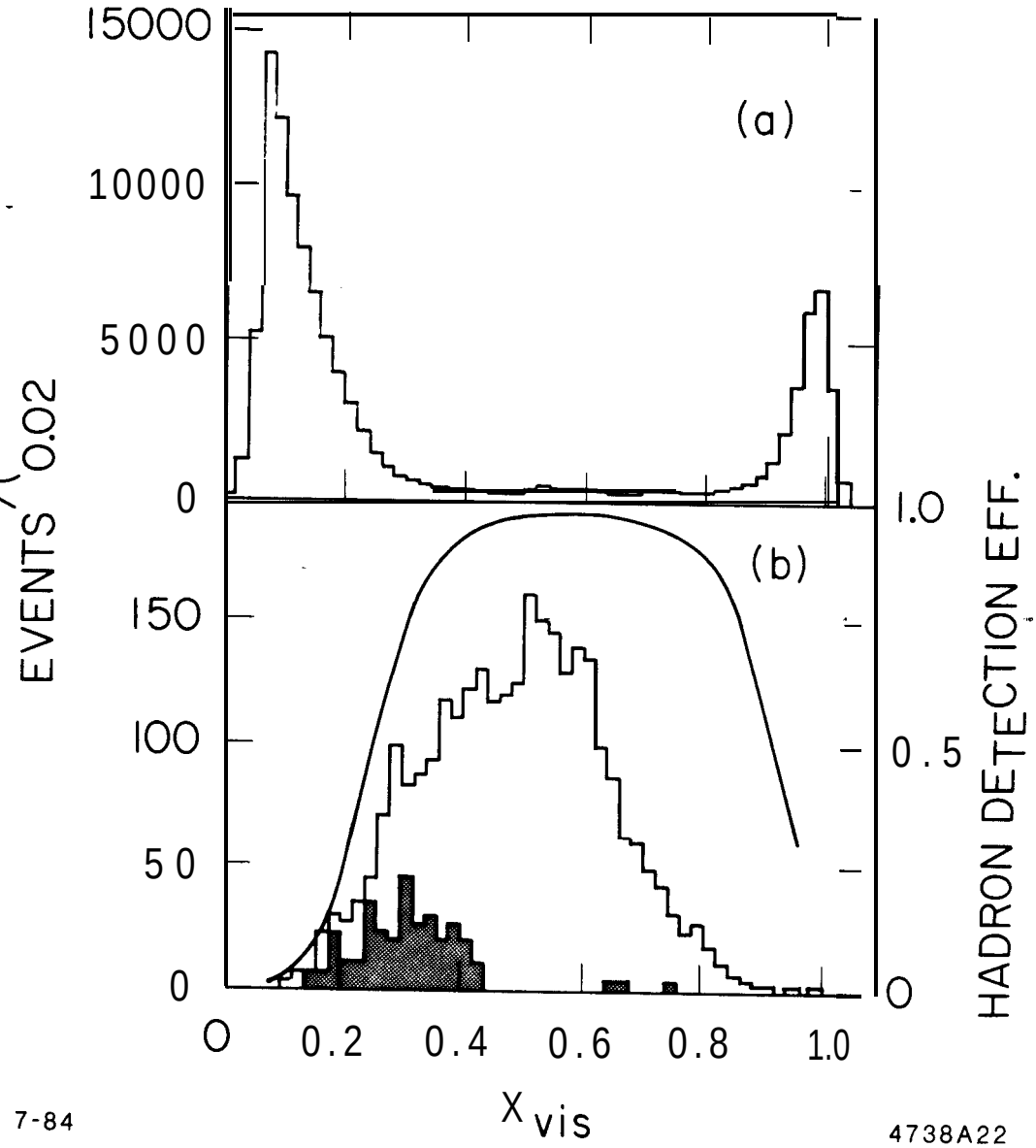
15000
10000
5000
0
(a)
EVENTS / 0.02
150
100
50
0
(b)
1.0
0.5
0
HADRON DETECTION EFF.
0
0.2
0.4
0.6
0.8
1.0
X vis
7-84
4738A22

Fig. 8

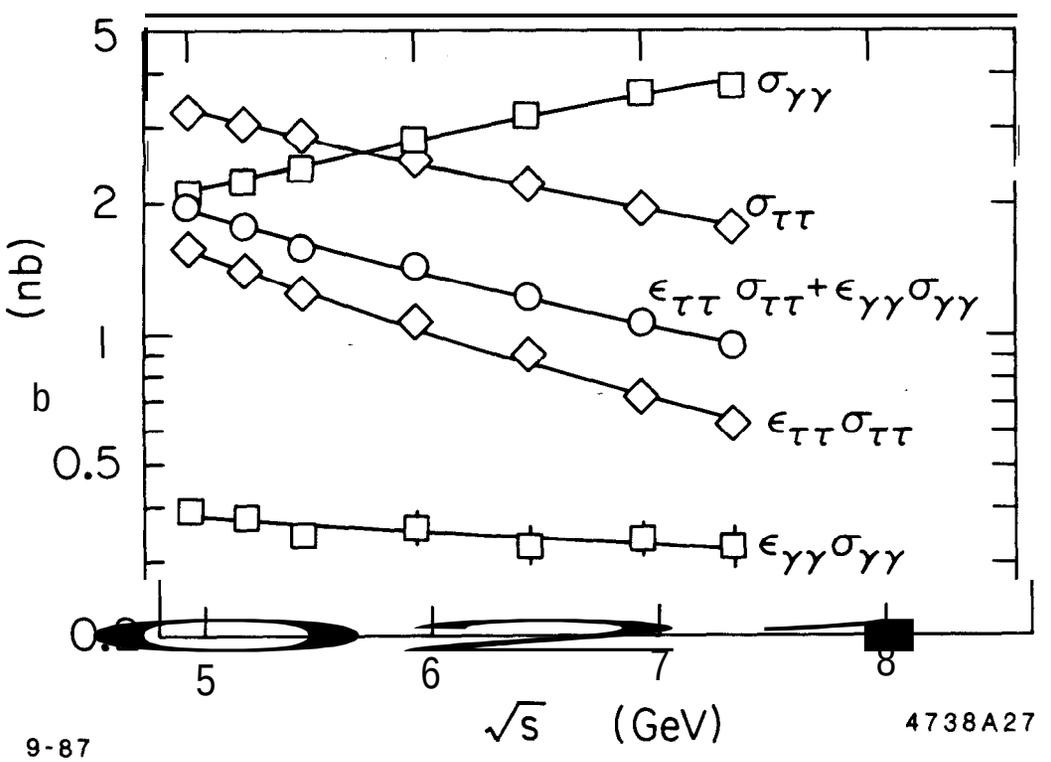
5
2
1
0.5
(nb)
b
$\sigma_{\gamma\gamma}$
$\sigma_{\tau\tau}$
$\epsilon_{\tau\tau}\sigma_{\tau\tau}+\epsilon_{\gamma\gamma}\sigma_{\gamma\gamma}$
$\epsilon_{\tau\tau}\sigma_{\tau\tau}$
$\epsilon_{\gamma\gamma}\sigma_{\gamma\gamma}$
5
6
7
8
$\sqrt{s}$ (GeV)
9-87
4738A27

Fig. 9

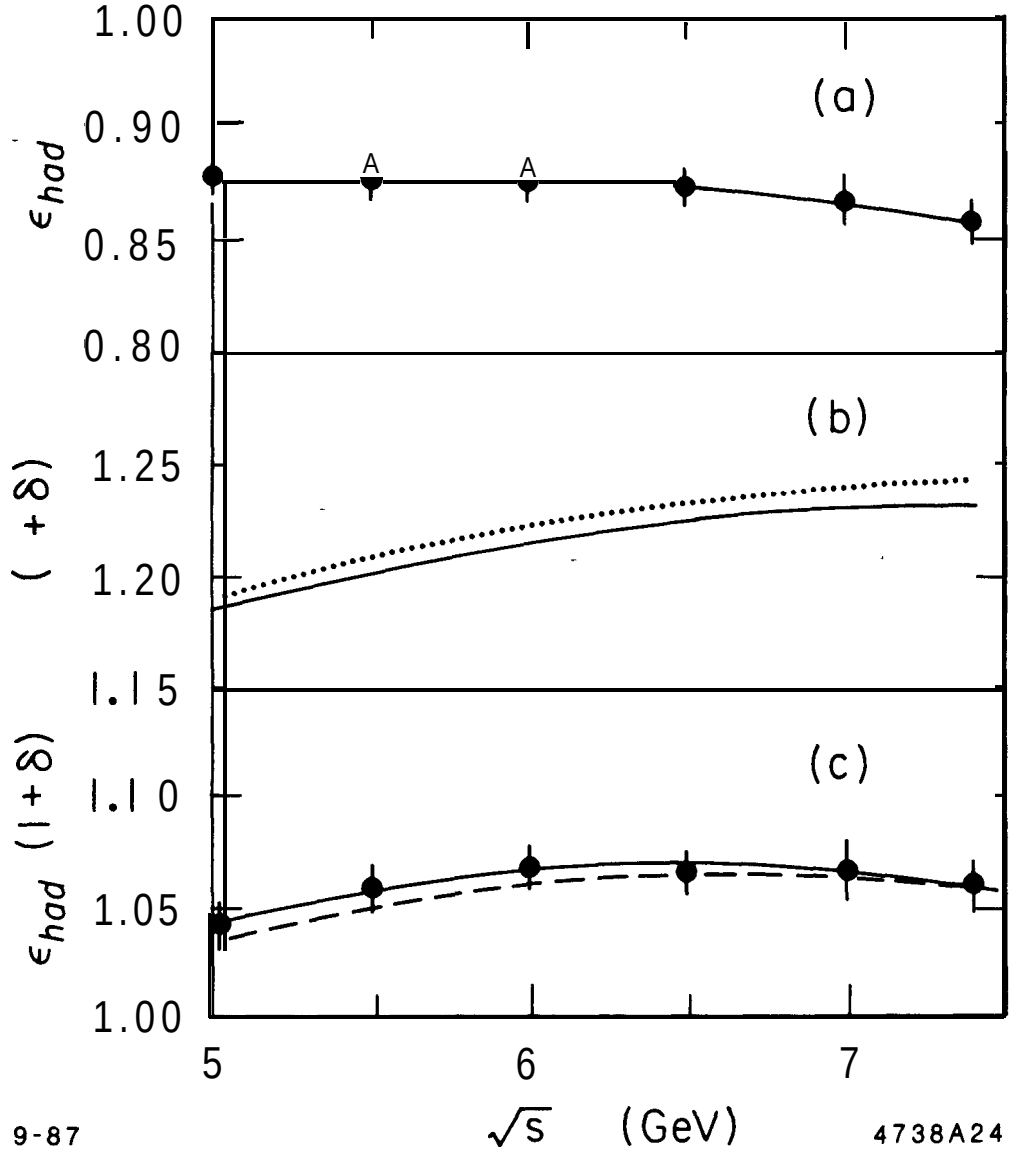
1.00
0.90
0.85
0.80
(a)
ϵ_{had}
A
A
(b)
$(1+\delta)$
1.25
1.20
1.15
(c)
$\epsilon_{had}\ (1+\delta)$
1.10
1.05
1.00
5
6
7
$\sqrt{s}$ (GeV)
9-87
4738A24

Fig. 10

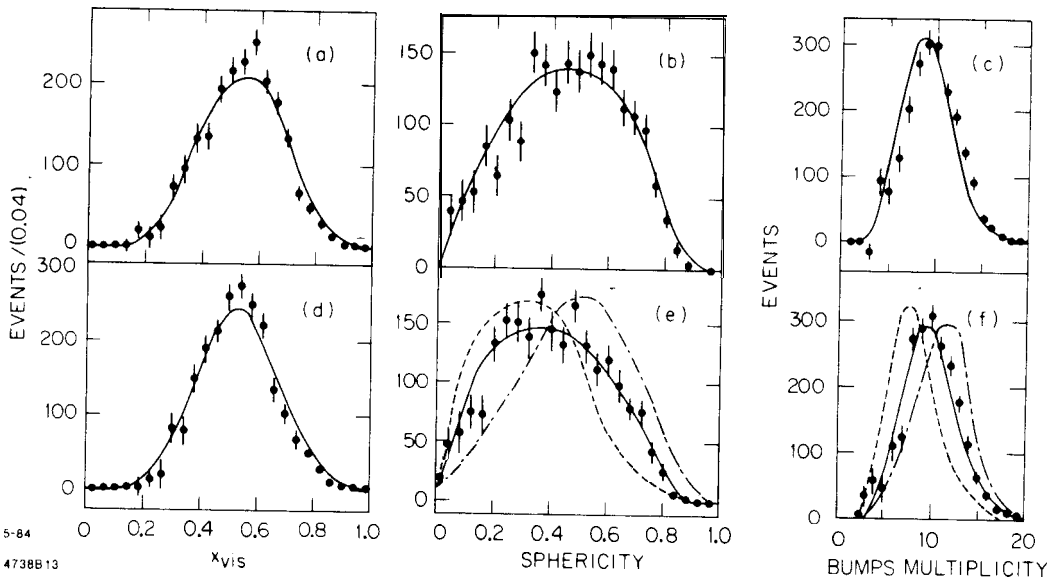
(a)
(b)
(c)
(d)
(e)
(f)
EVENTS /(0.04)
EVENTS
x_{vis}
SPHERICITY
BUMPS MULTIPLICITY
5-84
4738B13

Fig. 11

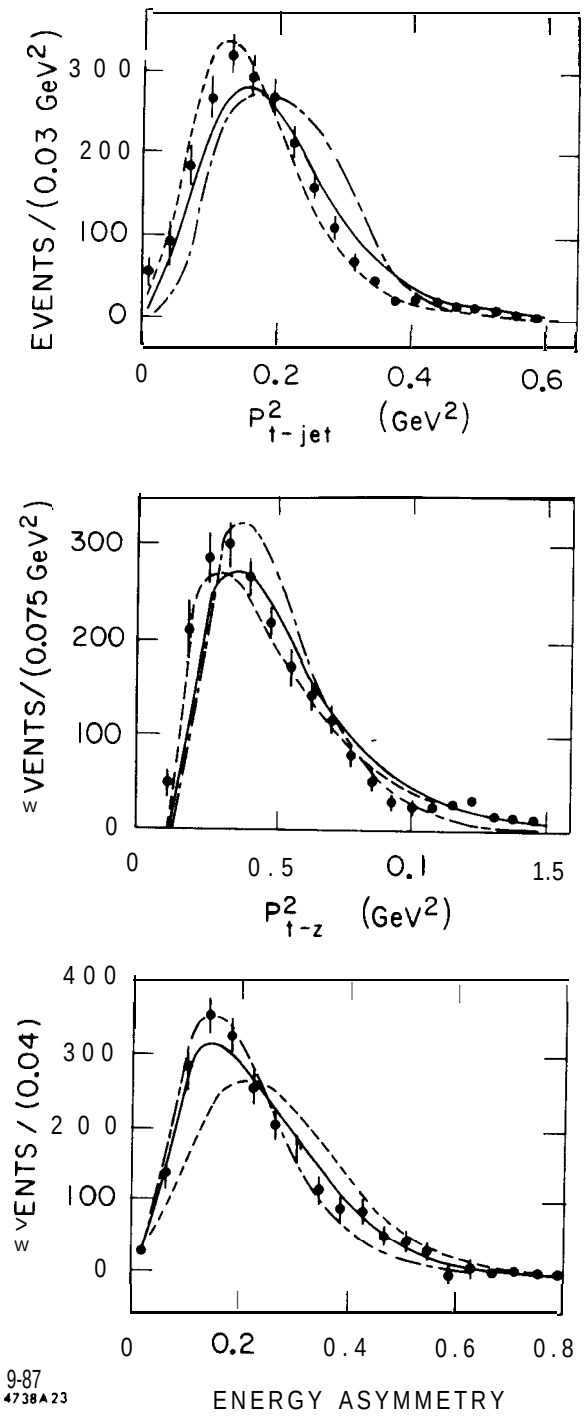
EVENTS/(0.03 GeV²)
300
200
100
0
0
0.2
0.4
0.6
P²t-jet (GeV²)
EVENTS/(0.075 GeV²)
300
200
100
0
0
0.5
0.1
1.5
P²t-z (GeV²)
EVENTS / (0.04)
400
300
200
100
0
0
0.2
0.4
0.6
0.8
ENERGY ASYMMETRY
9-87
4738A23

Fig. 12

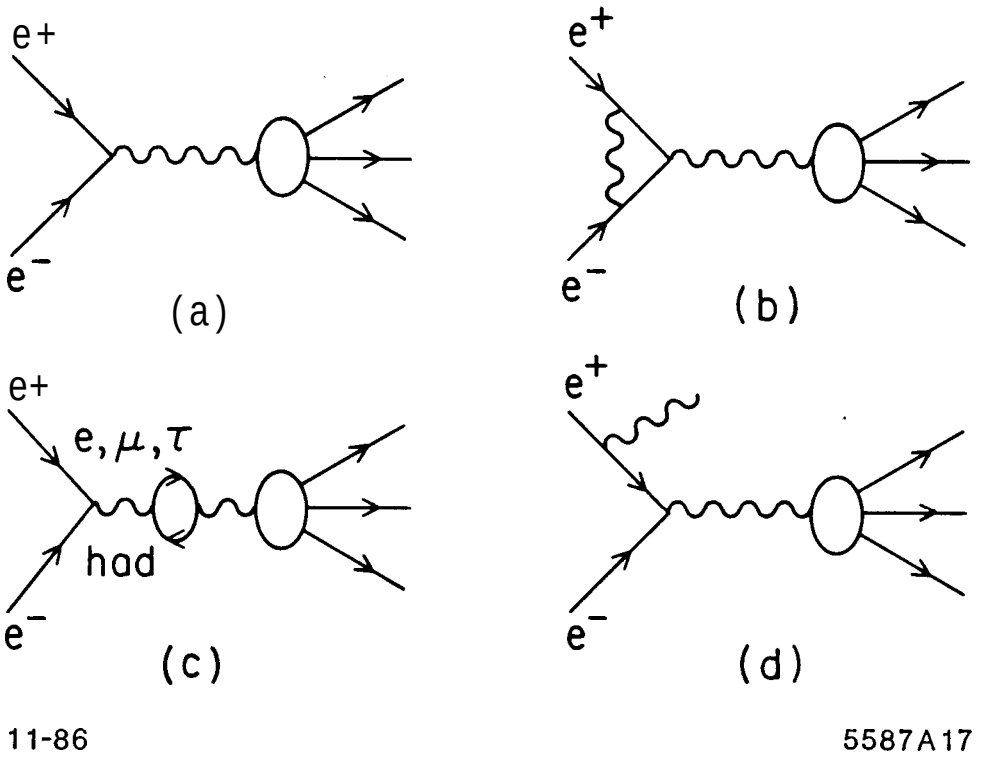

Fig. 13

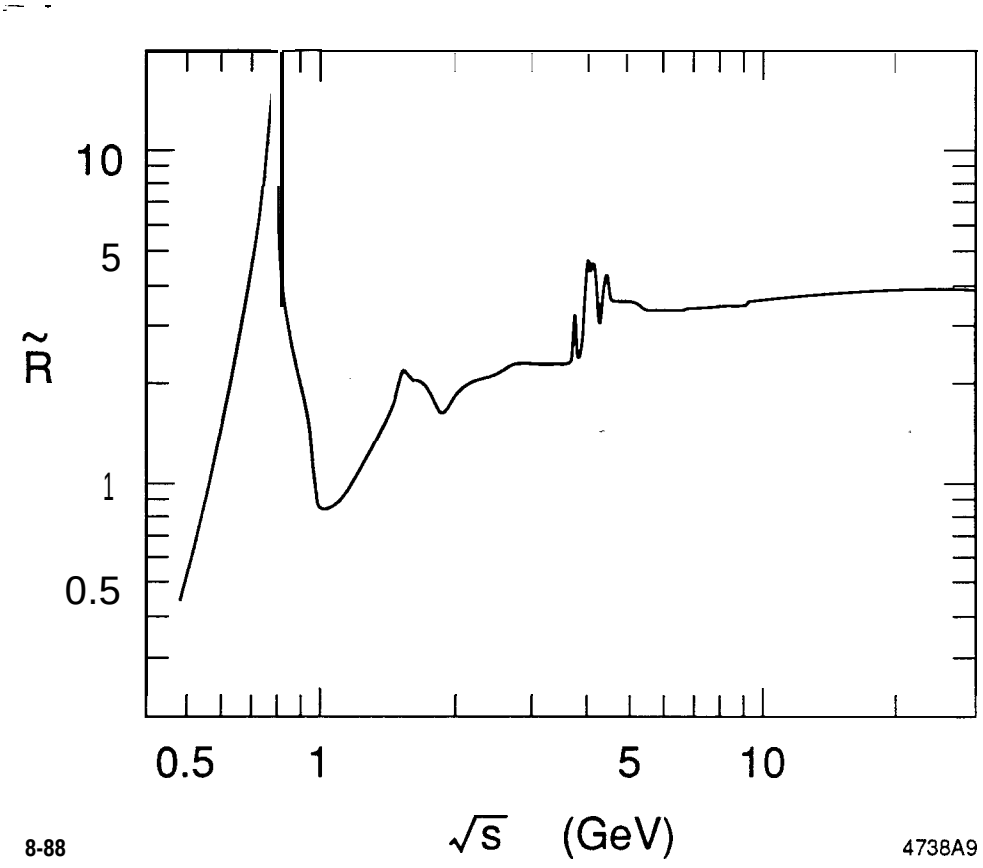

Fig. 14

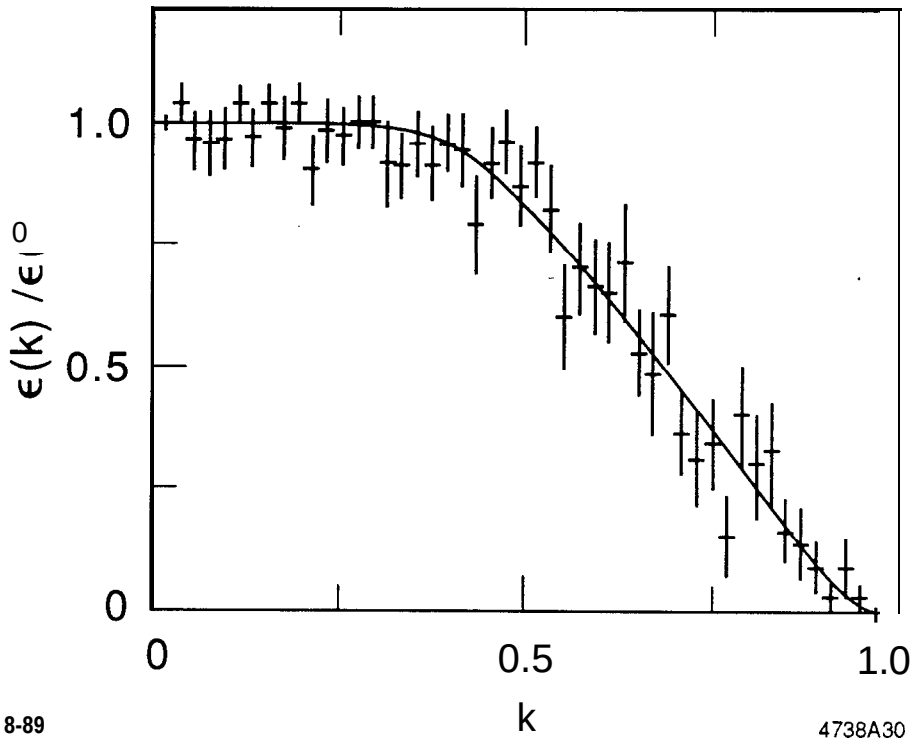

Fig. 15

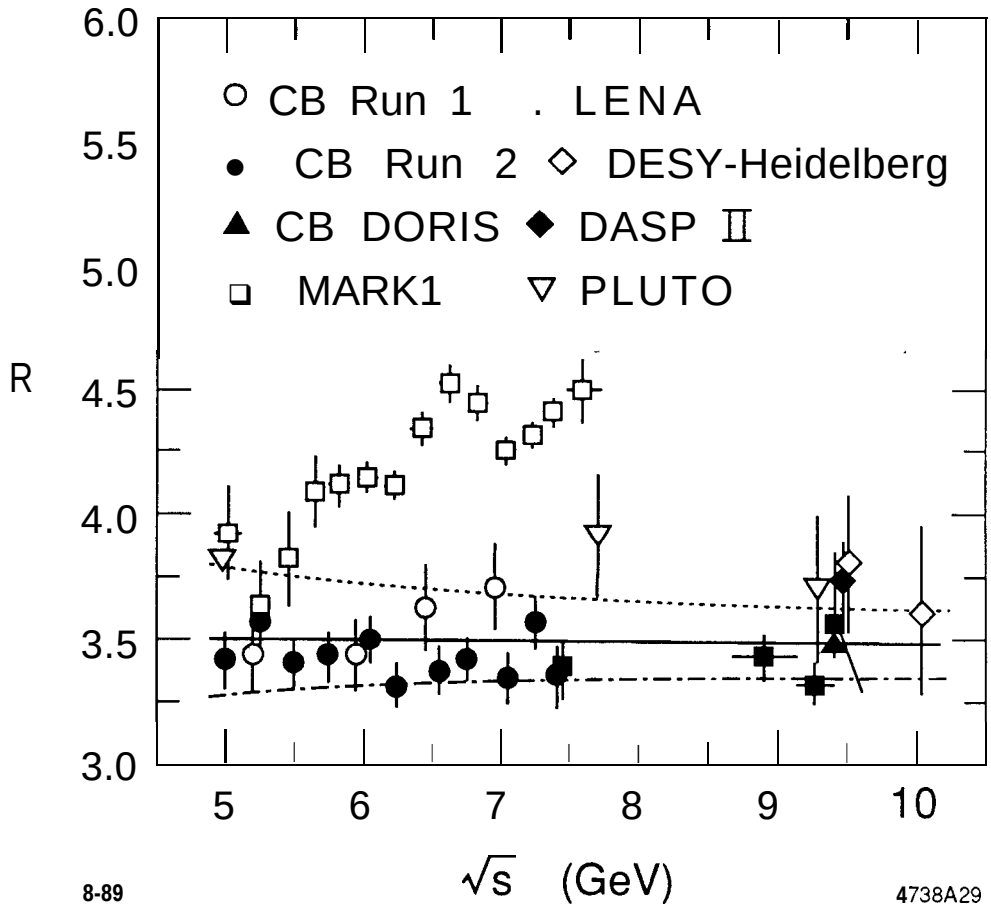
6.0
5.5
5.0
4.5
4.0
3.5
3.0
R
CB Run 1 . LENA
CB Run 2
DESY-Heidelberg
CB DORIS
DASP II
MARK1
PLUTO
5
6
7
8
9
10
√s (GeV)
8-89
4738A29

Fig. 16